1 **LARGE, an AMPA receptor interactor, plays a large role in long-term**

2 **memory formation by driving homeostatic scaling-down**

3

4 Bo Am Seo[2,], Taesup Cho[1], Daniel Z. Lee[3], Hwa Young Lee [1], Joong-Jae Lee[1], Boyoung

5 Lee[1], Seong-Wook Kim[1], Kathryn A. Cunningham[4,5], Kelly T. Dineley[4,6], Thomas A. Green[4,5],

6 Ho Min Kim[2], Se-Young Choi[7], Hee-Sup Shin[1], and Myoung-Goo Kang[1,2,3,4,*]

7

8 [1]Center for Cognition and Sociality, Institute for Basic Science (IBS), Daejeon 34141,

9 Republic of Korea

10 [2]Biomedical Science & Engineering Interdisciplinary Program, Korea Advanced Institute of

11 Science and Technology (KAIST), Daejeon 34141, ROK

12 [3]Department of Neuroscience and Cell Biology, [4]Center for Addiction Research,

13 [5]Department of Pharmacology &Toxicology, [6]Department of Neurology, University of Texas

14 Medical Branch (UTMB), Galveston, TX 77555, USA

15 [7]Department of Physiology, Seoul National University School of Dentistry, Seoul 03080,

16 Korea

17

18

19 *Correspondence: mkang13@gmail.com

Abstract

Dynamic trafficking of AMPA-type glutamate receptor (AMPA-R) in neuronal cells is a key cellular mechanism for learning and memory in the brain, which is regulated by AMPA-R interacting proteins. LARGE, a protein associated with intellectual disability, was found to be a novel component of the AMPA-R protein complex in our proteomic study. Here, our functional study of LARGE showed that during homeostatic scaling-down, increased LARGE expression at the Golgi apparatus (Golgi) negatively controlled AMPA-R trafficking from the Golgi to the plasma membrane, leading to downregulated surface and synaptic AMPA-R targeting. In *LARGE* knockdown mice, long-term potentiation (LTP) was occluded by synaptic AMPA-R overloading, resulting in impaired long-term memory formation. These findings indicate that the fine-tuning of AMPA-R trafficking by LARGE at the Golgi is critical for memory stability in the brain. Our study thus provides novel insights into the pathophysiology of brain disorders associated with intellectual disability.

Introduction

LARGE is expressed strongly in the brain (particularly the hippocampus), relative to other tissues(**Peyrard et al., 1999**). In humans, mutations in *LARGE* are associated with congenital muscular dystrophy type 1D, which is characterized by clinical features including profound intellectual disability, abnormal electroretinogram findings, and subtle structural brain abnormalities (**Clarke et al., 2011; Longman et al., 2003; Vaillend et al., 2008; Lisi and Cohn, 2007**). *Large^{myd}* mice, which carry a natural truncation mutation of *LARGE*, exhibit a number of neurological phenotypes, including sensorineural deafness and defective retinal transmission, along with developmental brain abnormalities (**Holzfeind et al., 2002; Michele et al., 2002**) and impaired long-term potentiation (LTP) (**Satz et al., 2010**). These human and mouse studies suggest that abnormal synaptic function may be responsible for intellectual disabilities in human patients with *LARGE* mutations.

In our previous proteomic analysis, we found that LARGE forms a protein complex with the AMPA-type glutamate receptor (AMPA-R) (**Kang et al., 2012**). Excitatory glutamatergic synaptic transmission within the central nervous system is primarily mediated by AMPA-R, as well as NMDA-type glutamate receptor (NMDA-R), and increasing numbers of proteins have been found to form complexes with and thus regulate the dynamic trafficking of AMPA-R. This tight regulation of AMPA-R trafficking in and out of the synapses, mediated by AMPA-R interactors, is widely considered to be a central brain mechanism involved in information storage (**Hanley, 2010**).

Changes in neuronal activity can alter synaptic transmission efficacy. This phenomenon, known as synaptic plasticity, is a main mechanism underlying learning and memory in the brain. Several forms of synaptic plasticity, including Hebbian, homeostatic, and structural, have been identified. Hebbian synaptic plasticity involves acute adaptations of neurons in

3

60   the brain during learning and memory processes (including LTP), wherein repeated neuronal

61   stimulation causes changes in synaptic efficacy. Homeostatic synaptic plasticity involves the

62   chronic adaptation of neurons against prolonged changes in neuronal activity and is required

63   for stability of encoded memory in the brain. Structural synaptic plasticity describes changes

64   in the lengths, shapes, and numbers of neuronal dendrites and dendritic spines. Notably,

65   AMPA-R trafficking plays critical roles in all three types of synaptic plasticity. Therefore, our

66   understanding of synaptic plasticity, learning and memory, and cognitive brain function relies

67   on knowledge about the molecular mechanisms underlying AMPA-R trafficking regulation

68   (**Huganir and Nicoll, 2013**).

69   Our functional study of LARGE revealed a novel and robust cellular mechanism

70   underlying AMPA-R trafficking from the Golgi to the cell surface, which contributes to all

71   three types of synaptic plasticity. LARGE is necessary for synaptic scaling-down, a type of

72   homeostatic plasticity. Specifically, it downregulates the synaptic targeting of AMPA-R by

73   negatively modulating AMPA-R trafficking from the Golgi to the cell surface. Synaptic AMPA-

74   R overloading due to LARGE deficiency causes hippocampal LTP occlusion and the

75   abnormal enlargement of dendritic spines, resulting in abrogated long-term memory

76   formation. LARGE thus contributes to the stability of encoded memory by fine-tuning AMPA-

77   R trafficking at the Golgi in the hippocampal neurons.

78

79

80   .

81

82

4

83   **Results**

84

85   **LARGE is necessary for neuronal homeostatic scaling-down**

86   Previous studies of LARGE have suggested a role for this protein in synaptic plasticity

87   (**Clarke et al., 2011; Holzfeind et al., 2002; Lisi and Cohn, 2007; Longman et al., 2003;**

88   **Michele et al., 2002; Peyrard et al., 1999; Satz et al., 2010; Vaillend et al., 2008**). Our

89   proteomic study identified LARGE as a component of the AMPA-R protein complex (**Kang**

90   **et al., 2012**), a major player in synaptic plasticity via dynamic trafficking in and out of the

91   neuronal surface and synapse. To determine whether LARGE could regulate AMPA-R

92   trafficking, we selected a homeostatic scaling method that would allow the monitoring of

93   surface and synaptic AMPA-R trafficking in response to changes in neuronal activity

94   (**Turrigiano, 2008**).

95   First, we monitored LARGE protein expression in cultured hippocampal neurons treated

96   with either tetradotoxin (TTX) or bicuculline for 48 h to induce homeostatic scaling-up and

97   scaling-down, respectively (**Turrigiano, 2008**), which were confirmed by monitoring

98   changes in GluA1 surface localization (i.e., expected increases and decreases in response

99   to TTX or bicuculline treatment, respectively) through cell surface biotinylation. Interestingly,

100   bicuculline treatment led to a significant increase in LARGE expression, whereas TTX had

101   no effect on LARGE (**Figure 1A and Figure 1-figure supplement 2A**). We more carefully

102   analyzed this increase in LARGE expression from 0 to 72 h after bicuculline treatment and,

103   excitingly, observed an inverse correlation between LARGE and surface GluA1/2 expression

104   (**Figure 1B**). These results strongly suggest an association between increased LARGE

105   expression and decreased AMPA-R surface localization. To test this possibility, we altered

106   LARGE expression using adeno-associated virus (AAV) expressing short hairpin (sh) RNA

5

107   and rescue constructs (**Figure 1C**) after validating the efficacy of shRNA-mediated *LARGE*

108   KD (**Figure 1-figure supplement 1**). Notably, the bicuculline-induced decrease in surface

109   GluA1 was mitigated by *LARGE* KD but reversed by *LARGE* rescue (**Figure. 1C**). However,

110   neither LARGE KD nor LARGE rescue affected the TTX-induced increase in surface GluA1

111   (**Figure 1-figure supplement 2B**).

112   Next, we monitored changes in synaptic AMPA-R in a single cell level by measuring the

113   miniature excitatory postsynaptic current (mEPSC) at 48 h after bicuculline or TTX treatment

114   with or without *LARGE* shRNA or rescue (**Figure 1D and Figure 1-figure supplement 2C**).

115   Here, *LARGE* KD mitigated the bicuculline-induced decrease in synaptic AMPA-R according

116   to changes in mEPSC amplitude, and *LARGE* rescue reversed this occlusion (**Figure 2D**).

117   Again, neither *LARGE* KD nor *LARGE* rescue affected the TTX-induced increase in synaptic

118   AMPA-R (**Figure 1-figure supplement 2C**). The fidelity of our mEPSC experiments was

119   verified by monitoring cell batch-to-batch variation (**Figure 1-figure supplement 3**).

120   These data strongly suggest that LARGE is necessary for homeostatic scaling-down in

121   hippocampal neurons.

122

123   **LARGE downregulates AMPA-R surface localization**

124   LARGE is required for AMPA-R surface and synaptic targeting during homeostatic scaling-

125   down **(Figure 1)**. The inverse correlation between LARGE and surface GluA1/2 expression

126   **(Figure 1B)** suggests a link between increased LARGE expression and decreased AMPA-

127   R surface localization, and recent studies have indicated that AMPA-R synaptic targeting is

128   mainly regulated by the abundance of surface AMPA-R (**Granger et al., 2012; Hanley,**

129   **2010**). Accordingly, we hypothesized that LARGE drives synaptic scaling-down by

130   downregulating AMPA-R surface targeting, and we first investigated whether LARGE could

131   downregulate the cell-surface localization of AMPA-R (**Figure 2**).

132   Our surface biotinylation approach demonstrated significant increases and decreases in

133   AMPA-R surface localization in response to *LARGE* KD and rescue, respectively, whereas

134   KD or rescue affected total AMPA-R expression or NMDA-R surface localization (**Figure.**

135   **2A**). We additionally evaluated AMPA-R surface localization *ex vivo* using membrane-

136   impermeable bis(sulfosuccinimidyl) suberate (BS^3), which crosslinks proteins exposed on

137   the cell surface (**Figure 2B**). The molecular weight of cross-linked surface GluA1 (>250 kDa)

138   was higher than that of intracellular GluA1 (~105 kDa), consistent with our previous study

139   (**Lee et al., 2012**). Although the surface and intracellular GluA1 levels respectively increased

140   and decreased significantly in *Large*$^{\text{myd-/-}}$ mice relative to wild-type mice, NMDA-R surface

141   localization was not affected by LARGE deficiency (**Figure 2B**), further confirming that

142   LARGE specifically modulates AMPA-R. The increased AMPA-R surface localization

143   following *LARGE* KD was originated in a single cell level (**Figure 2C**).

144   We further investigated whether LARGE could modulate AMPA-R surface localization in

145   heterologous expression system. Here, in HEK293T cell culture, LARGE overexpression led

146   to strong decreases in surface GluA1 and GluA2 localization but did not affect total AMPA-

147   R expression (**Figure 2D**). The observed greater decrease in GluA1 relative to GluA2

148   (**Figure 2D**) may explain the greater decrease in surface GluA1 vs. GluA2 during synaptic

149   scaling-down (**Figure 1B**). Again, the effect of LARGE overexpression on AMPA-R surface

150   localization was recapitulated in individual hippocampal neurons (**Figure 2E**).

151

152   **LARGE upregulates the Golgi localization of AMPA-R**

7

153   Next, we used confocal imaging to assess the subcellular localization of LARGE and thus

154   understand the mechanism by which LARGE downregulates AMPA-R surface targeting.

155   LARGE is known to localize at the Golgi in heterologous cells (**Brockington et al., 2005**)

156   and to function at the Golgi in myocytes (**Kanagawa et al., 2004**). Similarly, in cultured

157   hippocampal neurons, we observed a major pool of LARGE at the Golgi and Golgi outposts

158   (**Figure 3A**). Accordingly, we hypothesized that LARGE downregulates AMPA-R trafficking

159   from the Golgi to cell surface by increasing AMPA-R localization at the Golgi.

160   To test this concept, we first analyzed the co-localization of GluA1 with the Golgi marker

161   GM130 in cultured hippocampal neurons after manipulating LARGE expression. Confocal

162   imaging demonstrated that *LARGE* KD significantly decreased the pool of GluA1 at the Golgi,

163   whereas *LARGE* rescue reversed this phenomenon (**Figure 3B**). Similarly, in HEK293T

164   cells, LARGE overexpression significantly increased AMPA-R localization at the Golgi

165   (**Figure 3-figure supplement 1A**).

166   Next, we biochemically analyzed the effects of LARGE co-expression on subcellular

167   AMPA-R localization by fractionating subcellular organelles from HEK293T cells transfected

168   with GluA1 without (-LRG) or with LARGE (+LRG) (**Figure 3C**). Without LARGE co-

169   expression, the major GluA1 pool was detected in fractions enriched for P-cadherin, a

170   plasma membrane marker. With LARGE co-expression, however, the major GluA1 pool

171   shifted to high-density fractions enriched for GM130, a Golgi marker. Furthermore, the

172   distributions of GluA1 and LARGE in the gradient almost completely overlapped when the

173   proteins were co-expressed (**Figure 3C**), indicating a strong and direct association.

174   Moreover, the relative AMPA-R pool size in the Golgi fractions decreased significantly in the

175   brains of *LARGE* KO mice relative to wild-type mice, whereas the relative pool size in the

176   plasma membrane fractions increased significantly (**Figure 3D and Figure 3-figure**

177   **supplement 1B**). These results suggest that LARGE plays an important role in maintaining

178   AMPA-R pools at the Golgi.

179

180   **LARGE associates with AMPA-R through direct interaction**

181   HEK293T cells do not express synaptic proteins. Therefore, the co-sedimentation and co-

182   localization of GluA1 with LARGE in these cells (**Figure 3C** and **Figure 3-figure**

183   **supplement 1A**) suggested a direct interaction. To test this possibility, we performed

184   reciprocal co-immunoprecipitation (co-IP) of LARGE and AMPA-R from HEK293T cells.

185   Both co-IP strategies consistently showed that LARGE could specifically bind to AMPA-R in

186   non-neuronal cells that do not express other known AMPA-R-binding proteins (**Figure 3E**).

187   Interestingly, in a co-IP of LARGE with GluA2, LARGE bind only to the GluA2 correspond to

188   intracellular GluA2 (**Hall et al., 1997**) (**Figure 3-figure supplement 2A**), suggesting that

189   LARGE binds with AMPA-R within the cell, likely at the Golgi.

190   We further reconstituted the interaction of LARGE with AMPA-R *in vitro* using an enzyme-

191   linked immunosorbent assay (ELISA) (**Figure 3F,G**). Given the molecular structures and

192   topologies of LARGE and GluA1, we hypothesized that the C-terminal ectodomain of

193   LARGE would bind the N-terminal ectodomain of GluA1. After confirming the purification of

194   each protein (**Figure 3-figure supplement 2B-E**), we constructed an ELISA assay to verify

195   the specific and direct interaction of LARGE with GluA1 (**Figure 3F**). Notably, GluA1 bound

196   to LARGE with a higher affinity relative to that exhibited by GluA2 or GluA4 (**Figure 3G**).

197   The interactions of LARGE with GluA1, 2, and 4 indicated that LARGE binding to AMPA-R

198   is not subunit-specific. Similarly, the binding of the other AMPA-R interacting proteins, such

199   as Stargazin (**Tomita et al., 2003**) and CKAMP44 is also not subunit-specific (**von**

200   **Engelhardt et al., 2010**).

9

201   As GluA1 binds directly to the LARGE ectodomains (including catalytic domains), we

202   evaluated whether the interaction of LARGE with AMPA-R could affect glycosylation of the

203   latter. However, we observed no dramatic changes in LARGE-mediated GluA1 glycosylation

204   (**Figure 3-figure supplement 3**), suggesting that the physical interaction of LARGE with

205   GluA1, rather than LARGE glycosyltransferase activity, is the essential element with respect

206   to AMPA-R. Similarly, a previous report found that the physical interaction of Notch with

207   OFUT1, a glycosyltransferase, rather than OFUT1 enzymatic activity, was essential to the

208   role of OFUT1 in Notch trafficking (**Okajima et al., 2005**). These results (**Figure 3**)

209   consistently demonstrate the ability of LARGE to interact directly and specifically with

210   AMPA-R to increase localization of the latter protein at the Golgi.

211

212   **The pool of LARGE-associated AMPA-R at the Golgi increases during homeostatic**

213   **scaling-down**

214   Next, we investigated whether LARGE-interacting AMPA-R at the Golgi might increase

215   during homeostatic scaling-down. Confocal imaging of cultured hippocampal neurons

216   revealed a significant increase in LARGE (**Figure 4A**) and accompanying increase in GluA1

217   at the Golgi (**Figure 4B**) at 48 h after bicuculline treatment, which also led to an increase in

218   GluA1 and LARGE co-localization around the perinuclear areas of neurons (**Figure 4C**).

219   Together, these data strongly suggest that the co-localization of GluA1 and LARGE at the

220   Golgi increases during synaptic scaling-down. Indeed, subcellular fractionation confirmed

221   increases in both GluA1 and LARGE at the Golgi during scaling-down (**Figure 4D**). Finally,

222   co-IP confirmed a significant increase in the association of LARGE with GluA1 during

223   bicuculline-induced synaptic scaling-down (**Figure 4E**). Although the amount of GluA1

224   immunoprecipitated by a GluA1 antibody decreased after bicuculline treatment, probably

225 because of increased protein (e.g., LARGE) binding and consequently reduced epitope

226 exposure, the amount of LARGE that co-immunoprecipitated with GluA1 remained

227 significantly elevated. Together, our results strongly support our working model, wherein

228 increased LARGE expression (in response to increased neuronal activity) negatively

229 regulates AMPA-R trafficking from the Golgi to the plasma membrane, thus downregulating

230 AMPA-R synaptic targeting during synaptic scaling-down (**Figure 4F**).

231

232 ***LARGE* KD impairs hippocampal LTP due to synaptic AMPA-R overload**

233 Previous studies of LARGE have suggested a role for this protein in Hebbian synaptic

234 plasticity (**Clarke et al., 2011; Holzfeind et al., 2002; Lisi and Cohn, 2007; Longman et**

235 **al., 2003; Michele et al., 2002; Peyrard et al., 1999; Satz et al., 2010; Vaillend et al.,**

236 **2008**), including LTP (**Satz et al., 2010**). The LTP deficit in *LARGE* KO mice could be due

237 to abnormal brain development such as neuronal migration defect (**Holzfeind et al., 2002;**

238 **Satz et al., 2010**). To determine whether the LARGE could affect Hebbian synaptic plasticity

239 in normally developed adult mouse brain, we investigated hippocampal synaptic plasticity

240 via *in vivo* LTP after KD of LARGE after the stereotaxic injection of an AAV expressing

241 *LARGE* shRNA with GFP. Theta-patterned stimulation (TPS) protocol (**Cho et al., 2013**)

242 readily induced long-lasting hippocampal CA1 LTP in control mice, but not in *LARGE* KD

243 mice (**Figure 5A**). Despite this LTP impairment, *LARGE* KD exhibited dramatic increases in

244 field excitatory postsynaptic potential (fEPSP) amplitudes (**Figure 5A**), leading us to analyze

245 these amplitudes at different stimulation intensities. In an input-output analysis, the AMPA-

246 R fEPSP amplitudes in *LARGE* KD mice increased significantly over input intensities of 30–

247 100 mV (). However, *LARGE* KD did not affect presynaptic neurotransmitter release and

248 short-term plasticity, which were evaluated using the paired-pulse ratio (PPR). The PPRs at

249   inter-pulse intervals of 200, 100, 75, 50, and 25 ms did not differ between control and *LARGE*

250   KD mice (**Figure 5-figure supplementary 1B**), suggesting that the synaptic changes

251   observed in the latter mice are not presynaptic events.

252   The above results strongly suggest that *LARGE* KD increases the synaptic current by

253   increasing the number of AMPA-R molecules at the postsynapses. We therefore further

254   examined whether LARGE could regulate the synaptic localization of AMPA-R. First, we

255   analyzed AMPA-R-mediated mEPSC in cultured neurons transfected with scrambled

256   shRNA, *LARGE* shRNA, or a *LARGE* rescue plasmid. *LARGE* KD significantly increased

257   the amplitude, but not the frequency, of mEPSC relative to the controls. Moreover, *LARGE*

258   rescue completely reversed the effect of KD on amplitude (**Figure 5B**). However, when we

259   tested the effect of *LARGE* KD on inhibitory synapses, we observed no change in the

260   miniature inhibitory postsynaptic current (mIPSC) in either *LARGE* KD or rescue cells

261   (**Figure 5-figure supplementary 1C**), consistent with the findings of a previous

262   study(**Pribiag et al., 2014**). These mEPSC and mIPSC analyses, therefore, demonstrate

263   that changes in LARGE expression specifically affect the number of synaptic AMPA-R

264   molecules at the excitatory postsynapses, without affecting presynapses or inhibitory

265   synapses.

266   Second, we subjected cultured hippocampal neurons to confocal imaging to demonstrate

267   that the number of GluA1 molecules within the dendritic spine increased significantly with

268   *LARGE* KD relative to control neurons, and this increase was reversed by *LARGE* rescue

269   (**Figure 5C**). Moreover, *LARGE* KD neurons had significantly larger spine heads but similar

270   spine densities relative to control neurons; again, this was reversed by *LARGE* rescue

271   (**Figure 5-figure supplementary 2**). Finally, our biochemical analysis demonstrated that

272   GluA1 expression in the postsynaptic density (PSD) increased significantly in the

273   hippocampi of *LARGE* KO mice relative to controls (**Figure 5D**). Altogether, the impaired

274   hippocampal LTP (**Figure 5A**) observed with *LARGE* KD is probably attributable to synaptic

275   AMPA-R overload (**Figure 5B-D**), which inhibits the further capacity to increase the synaptic

276   AMPA-R pool during LTP.

277

278   **LARGE deficiency impairs fear memory**

279   The effects of LARGE KD on Hebbian (LTP) and structural (spine size) synaptic plasticity

280   (**Figure 5**), which underlie learning and memory in the brain, strongly suggested a role for

281   LARGE in cognitive functions in the brain. To determine whether LARGE deficiency could

282   cause learning and memory problems in animals, we subjected *LARGE* KO (*Large^{myd-/-}*),

283   wild-type, and heterozygous mice (*Large^{myd+/-}* and ^{+/-}) to Pavlovian fear conditioning (**Figure**

284   **6A**) and observed similar freezing behaviors in all three groups (**Figure 6B**). One day after

285   fear conditioning, the mice were subjected to tests of contextual memory, an index of

286   associative memory dependent on both hippocampal and amygdala function, and cued

287   memory, a hippocampus-independent index of associative memory that still relies on proper

288   amygdala function (**Sanders et al., 2003**). Compared with wild-type mice, KO mice

289   displayed significant reductions in freezing behavior during both contextual and cued

290   memory tests (**Figure 6C,D**), indicating that *LARGE* KO leads to deficits in both

291   hippocampus- and amygdala-dependent memory.

292   We note, however, that KO mice are constitutive mutants. Therefore, the observed

293   memory deficits may be attributable to abnormal brain development. Accordingly, we

294   knocked down *LARGE* in the bilateral hippocampal CA1 regions of adult mice and rats via

295   the stereotaxic injection of an AAV expressing *LARGE* shRNA with GFP prior to Pavlovian

296   fear conditioning to examine the potential effects of LARGE on memory processes in the

13

297   absence of life-long inherent developmental abnormalities. Another group of mice injected

298   with AAV expressing scrambled shRNA with GFP served as a control. We subsequently

299   validated the efficacy of shRNA-mediated *LARGE* KD *in vivo* (**Figure 6-figure**

300   **supplementary 1**) and confirmed the reliability of the experimental animals used in fear

301   tests (**Figure 6-figure supplementary 2**). Although the two groups exhibited similar freezing

302   behavior (**Figure 6E**), *LARGE* KD mice exhibited significantly less freezing behavior during

303   contextual but not cued memory tests (**Figure 6F,G**). In rats, *LARGE* knockdown in the

304   hippocampal CA1 produced the same effects on memory (**Figure 6H–J**).

305

306   **LARGE deficiency impairs hippocampus-dependent long-term memory**

307   We next subjected *LARGE* KD mice to various memory tests to identify the specific memory-

308   associated role of LARGE in the brain. An initial open field test revealed no significant

309   differences between KD and control groups (**Figure 7A**). In other words, *LARGE* KD mice

310   exhibit normal locomotion and anxiety levels. To test spatial working memory, we used a Y-

311   maze to evaluate whether KD mice could remember which arms of the maze had been

312   recently visited. Again, no significant differences were observed between the groups (**Figure**

313   **7B**).

314   Next, we used a simple novelty preference test that has used in previous studies of GluA1

315   function for memory (**Freudenberg et al., 2016; Sanderson et al., 2009**), to measure both

316   short- and long-term spatial memory in *LARGE* KD mice, using inter-trial intervals of 1 min

317   and 24 h, respectively (i.e., hippocampus-dependent memory) (**Sanderson et al., 2009**).

318   Although both groups exhibited a similar degree of preference for the novel arm at 1 min,

319   the *LARGE* KD group failed to exhibit a preference for the novel arm at 24 h, compared with

320   the control group (**Figure 7C**).

321   Finally, we performed the novel object recognition test, a popular testing paradigm for

322   hippocampal function as a relay point of recognition memory (**Stilling et al., 2014**). During

323   the training session, both groups displayed similar degrees of preference for two equal

324   objects, with no inter-group difference in the short-term (5 min) preference for a novel object.

325   Over the long term (24 h), however, the *LARGE* KD group failed to display a preference for

326   the novel object relative to the control group (**Figure 7D**). Taken together, these findings

327   suggest that hippocampal *LARGE* KD specifically impairs long-term, but not short-term,

328   spatial and recognition memory.

329

330   **Discussion**

331   LARGE downregulates AMPA-R synaptic targeting by negatively controlling AMPA-R

332   trafficking from the Golgi to the plasma membrane, and thus fine-tunes synaptic AMPA-R

333   abundance (**Figure 4F**), a novel cellular mechanism underlying homeostatic scaling-down,

334   which is a form of homeostatic plasticity. Moreover, the fine-tuning of AMPA-R trafficking by

335   LARGE contributes to the two other types of synaptic plasticity, Hebbian (LTP) and structural

336   (spine size) synaptic plasticity, that are the main underlying mechanisms of learning and

337   memory. Indeed, hippocampus-dependent long-term memory formation was impaired in

338   LARGE knockdown mice. *LARGE* mutations are associated with intellectual disabilities in

339   humans (**Clarke et al., 2011; Longman et al., 2003; Vaillend et al., 2008**), and abnormal

340   homeostatic synaptic scaling has been suggested as a pathophysiological component of

341   brain disorders associated with maladaptive synaptic plasticity(**Turrigiano, 2008**). Our study

342   thus provides novel insights into psychiatric and neurological disorders associated with

343   intellectual disability.

15

344

345   **LARGE function for synaptic plasticity and memory stability.**

346   During homeostatic scaling-down, an increased LARGE expression at the Golgi apparatus

347   negatively modulated AMPA-R trafficking from the Golgi to the plasma membrane, leading

348   to the downregulation of surface and synaptic AMPA-R targeting. This novel mechanism for

349   the regulation of AMPA-R trafficking via Golgi explains how global synaptic scaling-down at

350   the single cell level is possible with all synapses regardless of their locations, connections,

351   and histories.

352   Both Hebbian and homeostatic synaptic plasticity mainly adjust synaptic strength by

353   altering the abundance of AMPA-R in the postsynaptic membrane. Although the common

354   output suggests crosstalk between homeostatic and Hebbian synaptic plasticity (**Turrigiano,**

355   **2008**), the mechanism of interaction within the same neuron remained unclear. The

356   emerging idea that homeostatic synaptic plasticity acts as a form of metaplasticity to

357   influence the subsequent induction of Hebbian plasticity (**Arendt et al., 2013; Soares et al.,**

358   **2013**) is supported by our study. The lack of scaling-down and consequent increased GluA1

359   synaptic targeting precluded the further synaptic addition of AMPA-R required for the

360   induction of LTP. Moreover, our study strongly suggested that the crosstalk is required to

361   stabilize encoded memories in the brain. A memory can be stabilized in the long-term

362   through a consolidation process. LARGE KD mice exhibit deficits not in short-term memory

363   but in long-term memory that needs consolidation **(Figure 7)**. Without the LARGE-mediated

364   scaling-down, synaptic AMPA-R levels increase chronically. The AMPA-R overload at the

365   synapse is similar to an unconstrained LTP status (**Turrigiano, 2008**), wherein memory

366   remains unstable because of a breakdown in synapse specificity. Together, our LARGE

16

367   functional study proposed a novel mechanism underlying the role of homeostatic synaptic

368   plasticity for memory stability.

369

370   **Function of LARGE in the hippocampal consolidation of long-term memory**

371   The fear memory deficit observed in *LARGE* KO and KD animals indicates a role for LARGE

372   in hippocampus-dependent memory (**Figure 6**). To determine a more specific function of

373   LARGE, we subjected hippocampal CA1 *LARGE* KD mice to working, spatial, and

374   recognition memory analyses. Working memory, which is necessary for the temporary

375   storage and manipulation of information required for complex cognitive tasks, involves the

376   hippocampal CA1 region (**Dillon et al., 2008**). The absence of *LARGE* KD-induced changes

377   in working memory (**Figure 7B**) indicated that LARGE affects a particular type of memory.

378   Next, we applied simple novelty preference and novel objective recognition tests to

379   respectively examine spatial and recognition memory in *LARGE* KD mice. The former test

380   identified an impairment in long- but not short-term spatial memory (**Figure 7C**). In simple

381   novelty preference test, spatial long-term memory is formed through repetitive training over

382   several days. This result thus suggests that LARGE plays a role in hippocampal memory

383   consolidation. Similarly, the novel objective recognition test revealed impairment in long-

384   rather than short-term object recognition in *LARGE* KD mice (**Figure 7D**). Working memory

385   is hippocampus-dependent (**Dillon et al., 2008**) but does not require consolidation (**Guitar**

386   **and Roberts, 2015**). Hence, the intact spatial working memory and short-term memory

387   observed in this study strongly suggest that hippocampal *LARGE* KD specifically affects

388   hippocampus-dependent, consolidation-requiring processes essential for memory stability.

389

390   **Effects of LARGE on Hebbian synaptic plasticity**

17

391   Hippocampal *LARGE* KD caused a failure of LTP (**Figure 5A**), which underlies long-term

392   memory formation (including spatial memory consolidation) (**Lynch, 2004; Nabavi et al.,**

393   **2014**). This LTP impairment was attributed to an overload of synaptic AMPA-R that blocked

394   further AMPA-R synaptic targeting (**Figure 5B–D and Figure 5-figure supplementary 1A**).

395   In consistent with our results, LTP occlusion due to elevation in postsynaptic AMPAR surface

396   expression and function was reported previously (**Traunmuller et al., 2016**). The synaptic

397   AMPA-R overload was due to chronic increase of neuronal activity (**Figure 4F**). Supportively,

398   previous studies have shown that abnormally increased synaptic activity impairs LTP and

399   memory. For example, enhanced synaptic responses suppress LTP development, resulting

400   in hippocampal memory deficits(**Barnes et al., 1994**), whereas chronically increased

401   fEPSPs cause persistent deficits in the acquisition of new spatial information (**Castro et al.,**

402   **1989; McNaughton et al., 1986**). However, short-term plasticity remained intact in *LARGE*

403   KD animals (**Figure 5-figure supplementary 1B**), consistent with the normal acquisition of

404   fear training and short-term memory in both KO and KD animals (**Figure 6,7**). These results

405   corroborate the theory that short- and long-term memories result from dissociable

406   physiological processes (**Spear and Miller, 1981**) and are formed by different

407   neurobiological mechanisms(**Barker et al., 2006**). The lack of change in short-term plasticity

408   also supports our hypothesis that LARGE has a postsynaptic, rather than presynaptic, effect

409   on synaptic plasticity, as demonstrated by the absence of effects of *LARGE* KD or

410   overexpression on mEPSC frequency (**Figure 5B**).

411   Studies of LARGE function in the brain have focused on the association of LARGE with the

412   dystrophin glycoprotein complex (DGC) (**Michele et al., 2002; Pribiag et al., 2014; Satz et**

413   **al., 2010**). DGC components, including dystroglycan, are specifically expressed in inhibitory

414   GABAergic synapses but not at excitatory glutamatergic synapses (**Levi et al., 2002;**

18

415 **Pribiag et al., 2014**). Accordingly, the effects of LARGE on Hebbian synaptic plasticity via

416 the regulation of AMPA-R abundance at excitatory synapses provides novel insights into the

417 intellectual disabilities associated with *LARGE* mutations in the brain.

418
419

Materials and Methods

Animal care and treatments

Experiments involving animals were performed in accordance with procedures approved by the Institutional Animal Care and Use Committee at the University of Texas Medical Branch (UTMB) and the Korea Advanced Institute of Science and Technology (KAIST). Care was taken to minimize the number of animals used and their discomfort. Colonies of $Large^{myd}$ mice originated from Jackson Laboratory and were transferred from Dr. Kevin Campbell's laboratory at the University of Iowa prior to establishment at UTMB. Male adult C57BL/6 mice (wild type) were used in this study. The Sprague–Dawley rats and C57BL/6 mice used for behavior tests and neuronal cell culture were purchased from Harlan (USA) or Orient (Korea).

HEK293T cell culture

HEK293T cells were cultured at 37ºC in high-glucose Dulbecco's Modified Eagle's Medium (Sigma) supplemented with 10% fetal bovine serum (Gibco) and antibiotics (Gibco). For transfection, cells were plated on coverslips in 12-well plates or 6-well plates and then transfected with various expression plasmids using the transfection reagent TransIT-X2 (Mirus #mir6000).

Neuronal culture

Hippocampal neuronal cultures were prepared and maintained with glia-conditioned media as previously described (Kang et al., 2009). Briefly, timed pregnant female C57BL/6 mice and Sprague–Dawley rats were purchased, and primary cells were isolated from embryonic

20

444   day 17–18 (E17–18) pups. Mixed cell cultures containing both neurons and glia were then

445   grown on coverslips in 12-well plates and in 6-well plates for use in biochemical experiments.

446   The cultures were treated with 5 μM cytosine β-D-arabinofuranoside (AraC, Sigma) at day

447   in vitro (DIV) 3 to reduce the number of glial cells.

448

449   <u>Preparation of cDNA, shRNA, virus, transfection</u>

450   The LARGE cDNA plasmid was kindly provided by Dr. Kevin Campbell (University of Iowa,

451   Iowa City, IA, USA) and has been described previously (Kanagawa et al., 2004). The shRNA

452   virus constructs were designed, generated, and screened as previously described (Kang et

453   al., 2009). Briefly, four siRNAs were designed using Custom *SMART*pool Design and

454   synthesized (GE Dharmacon). The knockdown efficacy of each siRNA was tested, and the

455   sequence of the selected siRNA (rat: CGGCUUUGCUGCCUUGAAA, mouse:

456   UGGCUUUGCUGCCUUGAAA) was used to design an shRNA. The *LARGE* rescue

457   construct was generated by replacing the sequence encoding GFP in the pAAV vector used

458   for *LARGE* knockdown with a *LARGE* cDNA containing a shRNA-resistant sequence

459   (CGGCUUUGCUGCC<u>U</u>UGAAA => CGGCUUUGCUGCC<u>C</u>UGAAA).

460   The AAV was packaged and purified as follows. The shRNA designed from the selected

461   siRNA sequence was subcloned into the pAAV vector, and subsequently packaged into the

462   virus by co-transfecting HEK293T cells with pHelper and pAAV-RC (serotype DJ/8). At 72 h

463   post-transfection, the viral particles were harvested through two freeze/thaw cycles and

464   sonication. Benzonase and Rnase I were added to the virus-released solution. To remove

465   cell debris, the cell lysates were centrifuged at 2500 × g for 15 min, and the supernatants

466   were filtered through 0.2-μm syringe filters (Millipore, USA). A stock solution of 2.5 N NaCl

467   and 40% PEG8000 (Sigma #5413) was added to the supernatant to yield final respective

21

468 concentrations of 0.5 N and 8%. The resulting solution was incubated on ice for 3 h and

469 centrifuged at 2000 × g for 30 min, after which the supernatant was discarded. The pellets

470 containing AAV were resuspended in HEPES buffer, and this crude AAV solution was

471 treated with chloroform and PEG for an aqueous two-phase extraction (10% PEG8000–13.2%

472 $(NH_4)_2SO_4$) and final dialysis. The titer ($>1 \times 10^{11}$ TU/ml) was measured by treating 10^6

473 neurons with the AAV and measuring enhanced green fluorescent protein (GFP) expression

474 after 1 week (Figures S1A). The knockdown efficacy of AAV was evaluated using western

475 blotting (Figures S1A).

476 Cell transfection procedures used the same shRNA constructs (pAAV) except for the rescue

477 construct. For these experiments, the *LARGE* rescue construct was generated by adding a

478 self-cleaving 2A peptide (P2A) site between the sequence encoding the *LARGE* cDNA

479 containing the shRNA-resistant sequence and enhanced GFP within the *LARGE* shRNA-

480 containing pAAV vector. The knockdown and rescue efficacies were evaluated using

481 confocal imaging.

482

483 <u>Reverse transcription polymerase chain reaction (RT-PCR)</u>

484 RNAs were extracted (MACHERY-NAGEL # MN740955.50) from the infected hippocampal

485 CA1. cDNAs were synthesized from these RNAs using a kit according to the manufacturer's

486 protocol (Invitrogen #11904-018). The genes (*LARGE*, *β-actin*) tested in this study were

487 amplified from cDNA using DNA polymerase (enzynomics #P525) and gene-specific primers

488 (in Key resource table).

489

490 <u>Stereotaxic injection of virus into animals</u>

22

491   Adult (9–10 weeks of age) male C57BL/6 mice and Sprague–Dawley rats (body weight:

492   275–300 g) were assigned to either a control or an experimental group and injected with

493   AAV expressing either scrambled or *LARGE* shRNA, respectively, with enhanced GFP.

494   Specifically, the animals were anesthetized with 2% avertin (Sigma) and placed into a

495   stereotaxic apparatus (David Kopf instruments), after which the virus solution was injected

496   into the bilateral CA1 region of the hippocampus using the following coordinates: mouse,

497   anteroposterior, -1.95 mm from bregma; mediolateral, ±1.39 mm; dorsoventral -1.66 mm;

498   rat, anteroposterior, -2.4 mm from bregma; mediolateral, ± 2.0 mm; dorsoventral -2.0 mm.

499   For mice, 0.5 µl of virus solution was injected using a *picospritzer* with a glass pipette

500   (diameter, 15–20 µm). For rats, 2 µl of virus solution was injected at a rate of 0.1 µl/min

501   using a syringe pump with a glass pipette (5-µl syringe), and the needle was left in place for

502   at least 10 min post-infusion. The animals were allowed to recover in a heated chamber

503   before waking and were used for behavior tests at least 3 weeks after virus injection. After

504   the tests, the targeting of virus injection into the hippocampal CA1 region was confirmed by

505   the digital imaging of brain slices (2 mm thick) under a blue LED flashlight (DFP-1; NightSea)

506   to excite the GFP. After detecting GFP fluorescence, the fluorescent region of the

507   hippocampus was dissected for biochemical analyses.

508

509   <u>Fear conditioning and fear memory tests</u>

510   Fear conditioning and fear memory tests were performed as previously described

511   (Hernandez et al., 2010). The two-pair model of fear conditioning involves placing the animal

512   in the fear conditioning apparatus (Med Associates) for a total of 7 min. Animals were left to

513   explore freely for 3 min. At the 3-min and 5-min time points, an acoustic conditioned stimulus

514   (white noise, 80 dB) was delivered for 30 s, and an unconditioned footshock stimulus was

515   administered through the grid floor during the last 2 s of tone presentation (0.5–0.6 mA for

516   mice, 0.8 for rats) and co-terminated with the tone. Contextual fear memory was evaluated

517   24 h after paired training by placing the animal into the same training context and measuring

518   freezing behavior for 5 min. The cued fear memory was evaluated at least 4 h after the

519   contextual test by placing the animal in a different context (novel cage floor, lighting, odor,

520   and visual cues) with a 3-min free exploration period. At the 3-min mark, the same acoustic

521   conditioned stimulus was delivered for 3 min, and freezing behavior was measured using

522   Actimetrics FreezeFrame software with real-time digital video. Data are expressed as the

523   percentage of freezing during each minute or as a mean across all minutes.

524

525   <u>Measurement of shock threshold</u>

526   The shock thresholds for flinching, jumping, and vocalization, which are used as indices of

527   sensitivity to a shock stimulus, were measured as previously described (Hernandez et al.,

528   2010). Each animal was placed in the fear conditioning apparatus, and a sequence of single

529   foot shocks was delivered. Initially, a 0.1-mA shock was delivered for 1 s; thereafter, the

530   shock intensity was increased by 0.1 mA at 30-s intervals until an intensity of 1.0 mA was

531   reached. The shock intensity was then decreased by 0.1 mA at 30-s intervals until an

532   intensity of 0.1 mA was reached. Thresholds were then quantified by averaging the shock

533   intensity at which each animal gave a flinching, jumping, and vocalization response.

534

535   <u>Open field test</u>

536   In mice, locomotor activity and anxiety-related behavior were measured using the open field

537   test. A mouse was placed in the corner of an open field box (40 cm × 40 cm × 40 cm; material,

538   white acryl). To evaluate locomotor activity, the total distance traveled (cm) was measured

539   during each 5 min of the 30-min test. To evaluate anxiety, the time spent in the center of the

540   box during the first 5 min (s) was analyzed (Ethovision XT 8.5, Nodulus). A photometer was

541   used to adjust the light within a range of 5–10 lux.

542

543   <u>Y-maze</u>

544   A Y-maze comprising of three symmetrical arms at 120° angles (30 cm length × 12 cm height

545   × 7 cm width) was constructed from opaque acryl. A mouse was placed in the center of the

546   maze and allowed to freely explore the three arms for 5 min. Timing began once the mouse

547   left the center. Arm entry was defined as having all four limbs inside an arm. The sequence

548   of entries was recorded to calculate spontaneous alternations.

549

550   <u>Simple novelty preference test</u>

551   The simple novelty preference test was performed as described previously (Sanderson et

552   al., 2009). The mice received five 2-min training trials involving exposure to two arms of a

553   Y-maze (Start and Other arms; the third arm is blocked). Short and long-term memory were

554   assessed by changing the interval between exposure training sessions. Timing was started

555   once the mouse left the start arm. After exposure training, mice were subjected to a novelty

556   preference test in which they were allowed to explore all three arms of the maze (Novel,

557   Start, and Other arms) for 2 min. The exposure trials and novelty preference test were each

558   separated by either 1 min (1-min inter-trial interval [ITI] condition) or 24 h (24-h ITI condition).

559   The novel arm preference was calculated as the percentage ratio of the total amount of time

560   spent exploring and number of entries into the Novel and Other arms (Novel/Novel + Other)

561   x 100%.

562

563   <u>Novel object recognition test</u>

564   The novel object preference test was performed as described previously (Stilling et al., 2014).

565   Mice were habituated to a white acryl box for 5 min on each of 2 consecutive days. Mice

566   were then habituated to the same two objects placed in corners of the box for 5 min on each

567   of the 2 consecutive days. The following day, the objects were exchanged for two new,

568   identical objects (A + A), and the mice were allowed to explore the objects for 5 min. Next,

569   the mice were placed in their home cages for 5 min (short-term memory task) and re-

570   exposed to the arena in which one object had been exchanged (A + B). After 24 h, B was

571   exchanged for C (long-term memory task). The durations of object contacts were measured.

572   The novel object preference was reported as: (novel / sum (both objects)) x 100%.

573

574   *In vivo* <u>field EPSP recordings</u>

575   Three to 4 weeks prior to *in vivo* field recording, AAV expressing *LARGE* shRNA with GFP

576   was infused into the hippocampal CA1 regions of adult C57BL/6 mice (8–9 weeks old) as

577   described in <u>*Stereotaxic injection of virus into animals*</u>. The stereotaxic unilateral injection of

578   0.5 µl of higher-titer AAV (1×10^{11} TU/ml) was performed using a stereotaxic, motorized

579   nano-injector (World Precision Instruments) at a rate of 0.1 µl/min via a Hamilton syringe

580   connected to a microinjection pump.

581   The fEPSPs from the hippocampal CA1 region were recorded as previously described (Cho

582   et al., 2013). C57BL/6 mice (n = 11–12) were anesthetized with urethane (1.6 g/kg, i.p.;

583   Sigma) and placed into a stereotaxic frame. Rectal temperature was maintained

584   intraoperatively at 36.5ºC ± 0.5ºC using a temperature controller (Harvard Instruments).

585   The scalp was opened and separated. Trephine holes were drilled into the skull, and

586   electrodes were positioned in the area of the hippocampal stratum radiatum. A bipolar

587   stimulating electrode (2.0 mm posterior to bregma, 2.0 mm lateral to midline) was used for

588   Schaffer collateral stimulation, and a monopolar recording electrode (1.9 mm posterior to

589   bregma, 1.4 mm lateral to midline) was used to record from the CA1 region. The final depths

590   of the electrodes were adjusted to optimize the magnitude of the evoked responses. The

591   fEPSPs were adjusted to 50–60% of the maximal response size for testing. Stimulation was

592   applied using an analog-to-digital interface (1322A; Molecular Devices) and a Digital

593   Stimulus Isolation unit (Getting Instruments). The pyramidal neuron responses to Schaffer

594   collateral stimulation were recorded using a differential amplifier (P55 A. C. pre-amplifier;

595   Grass Instruments) and analyzed using WinLTP software (WinLTP Ltd.). Responses were

596   evoked by single-pulse stimuli delivered at 20-s intervals. A stable baseline was recorded

597   for 30 min. LTP was induced by applying theta-patterned stimulation (TPS, four trains

598   comprising of 10 bursts of five pulses at 400 Hz with a 200-ms inter-burst interval and a 20-

599   s inter-trial interval) to the CA1 and was optimized based on previous studies (Cho et al.,

600   2013).

601

602   <u>Whole-cell patch-clamp recordings for mEPSCs and mIPSC analyses</u>

603   Cultured hippocampal neurons were prepared as described above. Using a calcium

604   phosphate transfection kit (Invitrogen #K278001), cultured hippocampal neurons were

605   transfected at DIV 8 with cDNA plasmids expressing either scrambled shRNA with enhanced

606   GFP, *LARGE* shRNA with GFP, or *LAEGE* shRNA with GFP and LARGE rescue. The

607   cultured neurons were used for electrophysiological recordings at 3 days post-transfection.

608   Miniature excitatory postsynaptic currents (mEPSCs) and miniature inhibitory postsynaptic

609   currents (mIPSCs) were recorded at room temperature (21–23ºC). Whole-cell voltage-clamp

610   recordings were performed using a multiclamp 700B amplifier (Molecular Devices), filtered

611   at 1 KHz, and digitized at 10 KHz (Digidata 1550; Molecular Devices). Recording pipettes

612   (4–6 MΩ) were filled with the following intracellular solutions, as appropriate: for mEPSC

613   analysis, 140 mM Cs-MeSO4, 8 mM NaCl, 10 mM HEPES, 0.5 mM EGTA, 1 mM $MgCl_2$, 4

614   mM Mg-ATP, 0.4 mM Na-GTP, 5 mM QX-314; for mIPSC analysis, 130 mM CsCl, 10 mM

615   NaCl, 1.1 mM EGTA, 2 mM $MgCl_2$, 0.1 mM $CaCl_2$, 10 mM HEPES, 2 mM Mg-ATP. The pH

616   was adjusted to 7.2 using CsOH, with 280–290 mOsm.

617   Hippocampal neurons on coverslips were transferred to a recording chamber that was

618   continuously perfused with extracellular solution (pH 7.4, 310–320 mOsm) containing 150

619   mM NaCl, 3.1 mM KCl, 2 mM $CaCl_2$, 1 mM $MgCl_2$, 10 mM HEPES, and 25 mM glucose. One

620   micromolar tetrodotoxin (Tocris Bioscience #1078), 50 µM DL-AP5 (Tocris Bioscience

621   #3693), and 100 µM picrotoxin (Sigma #P1675) were always included in the extracellular

622   perfusing solution for mEPSC (for mIPSC, 20 µM CNQX (Tocris Bioscience #0190) was

623   used instead of picrotoxin). All recordings were voltage clamped at -70 mV. Acquired data

624   were analyzed using pCLAMP 10.6 (Molecular Devices). Access resistance was

625   continuously monitored. The data were discarded if the R_a varied by >20% during recording.

626   Changes in frequency and amplitude were analyzed, quantified, and presented using traces,

627   cumulative plots, and scatter plots. We confirmed that the frequency and amplitude did not

628   vary among the batches used in experiments or between non-transfected and GFP-

629   transfected neurons (Cont). For the homeostatic synaptic scaling experiment, neurons were

630   pre-incubated in either 1 µM TTX or 20 µM bicucullin for 48 h before mEPSC recordings

631   were obtained as described above.

632

633   <u>Preparation of PSD</u>

634   PSD was prepared as described previously (Kang et al., 2012), with some modifications.

635

636   <u>Surface biotinylation</u>

637   HEK293T cells in 10-cm plates or cultured neurons in 6-well plates were washed with

638   phosphate-buffered saline (PBS) or artificial cerebrospinal fluid (ACSF; 0.15 M NaCl, 10 mM

639   HEPES, 3 mM KCl, 0.2 mM $CaCl_2$ dihydrate, 10 mM glucose), respectively, and placed on

640   ice. The cells were then incubated with 1–1.5 mg/ml sulfo-NHS-SS-biotin (Thermo #21331)

641   for 20 min at 10ºC. Subsequently, the biotin was quenched by incubation with 50 mM glycine

642   for 10 min on ice, followed by washing. The cells were removed by scraping and solubilized

643   in IP buffer containing 1.0% Triton X-100 and 0.1% SDS for 1 h at 4ºC. After solubilization,

644   the cells were centrifuged at 14,000 $\times$ g for 15 min, and the pellet was discarded. The

645   supernatant containing biotinylated proteins was incubated with NeutrAvidin-Sepharose

646   beads (Thermo #29200) for 3 h at 4ºC. The beads were then thoroughly washed with IP

647   buffer, and the proteins were eluted for 5 min at room temperature (RT) with protein gel-

648   loading buffer. The total and cell-surface proteins were analyzed by SDS-PAGE, followed

649   by western blot analysis.

650

651   <u>Analysis of cell-surface proteins in hippocampal slices using the cross-linking reagent BS[3]</u>

652   Cell-surface proteins were labeled using the membrane-impermeable cross-linking reagent

653   bis(sulfosuccinimidyl) suberate (BS[3], Thermo #21585) as described in previous studies (Lee

654   et al., 2012), with some modifications. After the cardiac perfusion of mice with cold ACSF,

655   the hippocampi were removed and placed into cold ACSF oxygenated with a 95% O_2/5%

656   CO_2 gas mixture. Each hippocampus was cut into five ~1-mm-thick slices and allowed to

657   float in oxygenated ACSF. Ten slices from two hippocampi were incubated in BS[3] (Thermo-

658   Pierce) solution (2.5 mM BS[3] dissolved in ACSF) for 40 min at 10ºC with gentle shaking.

659   After quenching with ACSF containing 100 mM glycine three times for 5 min each, the slices

660   were processed for solubilization, SDS-PAGE, and western blotting as described above for

661   surface biotinylation.

662

663   <u>Fractionation of subcellular organelles from cells or tissues</u>

664   The iodixanol-based iso-osmotic density gradient-based subcellular organelle fractionation

665   procedure was developed according to the instructions of the kit manufacturer (OptiPrep,

666   Sigma #D1556), and optimized for two scales (5-ml volume gradient and 0.7-ml volume

667   gradient). Briefly, cells or brain lysates were centrifuged for 10 min at 3000 × g, and the

668   pellet was discarded. The supernatant was then centrifuged for 1 h at 100,000 × g to remove

669   cytosolic contamination. The resulting second pellet was applied to the top of an OptiPrep

670   discontinuous iodixanol gradient formed by the stepwise addition of solutions with increasing

671   percentages of iodixanol (diluted in PBS). The 5.0-ml volume gradient was formed by adding

672   0.385 ml of 2.5%, 0.77 ml of 5%, 0.77 ml of 7.5%, 0.77 ml of 10%, 0.192 ml of 12.5%, 0.77

673   ml of 15%, 0.192 ml of 17.5%, 0.192 ml of 20%, and 0.192 ml of 30% iodixanol solutions to

674   the bottom of a 5-ml Beckman centrifuge tube. The 0.7 ml volume gradient was formed by

675   adding 27.5 µl of 30%, 27.5 µl of 20%, 27.5 µl of 17.5%, 110 µl of 15%, 27.5 µl of 12.5%,

676   110µl of 10%, 110 µl of 7.5%, 110 µl of 5%, and 55 µl of 2.5% iodixanol solutions to the

677   bottom of a 750-µl Beckman centrifuge tube. After centrifugation for 2 h at 150,000g in a

678   SW55i rotor and Beckman Optima centrifuge, 18–25 fractions were collected from the top

679   of the column, depending on the experimental condition. Proteins in the fraction sets were

680   resolved by SDS-PAGE, followed by western blot analyses with antibodies against the

681   proteins of interest, including organelle markers, LARGE, and GluA1. The proteins were

682   quantified by the densitometric analysis of bands in digital images of western blots and

30

683   subjected to statistical analyses. For each protein, the average density in each fraction was

684   normalized to the peak density of the protein and plotted as a line graph. For organelle

685   markers, each group was initially analyzed separately. However, as no significant changes

686   were observed between wild-type and mutant *Large*^{myd} mice, the data were subsequently

687   merged into a single group.

688

689   <u>Immunoprecipitation</u>

690   Small-scale immunoprecipitation was performed as described previously (Lee et al., 2012),

691   with some modifications.

692

693   <u>Western blot analysis</u>

694   Western blot analyses were performed as described previously (Kang et al., 2009). The

695   rabbit anti-LARGE antibody (Rb331) (Kanagawa et al., 2004) was characterized previously.

696   The mouse anti-β-actin (Sigma #A5441) and mouse anti-tubulin antibodies (Sigma #T9026)

697   were used at dilutions of 1:10000 and 1:20000, respectively. For organelle markers,

698   antibodies against rabbit anti-GM130 (Abcam #AB52649), mouse anti-TGN38 (Thermo

699   #MA3-063), and mouse anti-P-cadherin (Abcam #AB22744) were used at dilutions of

700   1:10000. Mouse anti-GluA1 (Millipore #MAB2263), rabbit anti-GluA2/3 (Millipore #07-598),

701   mouse anti-NR1 (Millipore #05-432), and rabbit anti-NMDAR2B antibodies (Abcam

702   #ab65783) were used at dilutions of 1:1000. Quantitative analyses of band intensities were

703   performed using Image Lab (Bio-Rad).

704

705   <u>Protein expression and purification of LARGE and Fc-fused GluA1Nt, 2Nt, and 4Nt for ELISA</u>

706   The gene encoding the human LARGE catalytic domain (CD1–CD2) was cloned into a

707   pET21a expression vector (Novagen) using the *NdeI* and *XhoI* restriction sites. The resulting

708   vector was transformed into Origami B (DE3) host cells (Novagen) to facilitate the formation

709   of disulfide bonds. Single colonies were seeded into LB media supplemented with ampicillin

710   (100 µg/ml), kanamycin (50 µg/ml), and tetracycline (15 µg/ml). After an overnight incubation,

711   10 ml of cultured cells were inoculated into 1,000 ml of fresh LB media. Once the cell density

712   at 600 nm reached approximately 0.5, isopropyl-d-1-thiogalactopyranoside (IPTG) and

713    $MnCl_2$ were added to final concentrations of 0.1 mM and 0.2 mM, respectively, to induce

714   protein expression. The induced cells were further cultured at 18ºC for 3 days. Following a

715   cell harvest via centrifugation at 6,000 rpm, the cell pellet was resuspended in lysis buffer

716   (20 mM Tris, 150 mM NaCl, 10 mM imidazole, pH 8.0) and subjected to disruption by

717   sonication. The sonicated lysate was subjected to ultracentrifugation at 13,000 rpm and 4ºC

718   for 1 hour, and the supernatant was filtered through a 0.2-µm syringe filter (Millipore) and

719   incubated with His-bind agarose resin (Elpis Biotech, Korea). After washing with a washing

720   buffer (20 mM Tris, 150 mM NaCl, 20 mM imidazole, pH 8.0), LARGE proteins were eluted

721   using an elution buffer containing 200 mM imidazole. Purified LARGE was subjected to a

722   buffer change to a Tris-based buffer (20 mM Tris, 150 mM NaCl, pH 8.0) supplemented with

723   0.2 mM $MnCl_2$. This solution was stored at 4ºC for further study.

724   Fc-GluA1Nt, 2Nt, and 4Nt were purified from HEK293T cells using a transient transfection

725   protocol. Cells were cultured in 10 cm x 15 cm plates to 85–90% confluency and transfected

726   with the target vectors (10 µg/plate). At 72 h post-transfection (Mirus), the cells were

727   harvested via centrifugation at 6,000 rpm, and the cell pellet was resuspended in PBS and

728   lysed by sonication. The lysate was then subjected to ultracentrifugation at 13,000 rpm and

729   4ºC for 1 hour, and the supernatant was filtered through a 0.2-µm syringe filter (Millipore)

730 and incubated with Protein A Sepharose beads (GE Healthcare #17-0780-01). After washing

731 with a washing buffer (0.5% Triton X-100, 0.5 mM EDTA, 0.5 mM in PBS), the target proteins

732 were eluted using an elution buffer containing 0.2 M glycine (pH 2.5). A proteinase inhibitor

733 was added to all purification steps. Purified LARGE was then subjected to a buffer change

734 using a Tris-based buffer (20 mM Tris, 150 mM NaCl, pH 8.0) and stored at 4ºC.

735

736 <u>Enzyme-linked immunosorbent assay (ELISA)</u>

737 A 96-well plate (SPL, Korea) was coated with purified LARGE protein and bovine serum

738 albumin (BSA) at 4ºC. The following day, the antigen-coated plate was washed with PBS

739 (pH 7.4) three times, and each well was incubated with a blocking buffer (PBS containing

740 0.1% Tween-20 and 2% BSA; PBST-BSA) at room temperature for 1 hour. All buffers used

741 in this study were supplemented with 2 mM MnCl$_2$. After three washes with PBST, 10 µg/ml

742 of Human-Fc fused GluA1 (GluA1-Fc) was added to the wells and incubated at room

743 temperature for 1 hour. To detect GluA1 binding to the LARGE-coated surface, the plate

744 was washed and incubated for 1 hour with goat anti-Human IgG (Fc specific)−Peroxidase

745 (Sigma #A0170) diluted 1:3,000 in PBST-BSA. Binding signals were developed and stopped

746 by the sequential addition of TMB (3,3',5,5'-tetramethylbenzidine) solution (Sigma #T0440)

747 and 1 N sulfuric acid, and the colorimetric reaction was evaluated by measuring the

748 absorbance at 450 nm. For a competition ELISA, GluA1-Fc was preincubated with 150 µg/ml

749 of soluble LARGE, a competitor, for 30 min before its addition to the LARGE-coated plate.

750 To identify binding preferences of LARGE toward the Fc-GluA1Nt, 2Nt and 4Nt subtypes,

751 different concentrations of GluA1-family proteins were applied to the LARGE-coated plates

752 as described above. The molarity of each subtype was calculated from the band intensity

753 and molecular weight.

33

754

755   Immunocytochemistry, microscopy, and image analyses

756   These processes were performed as described previously (Kang et al., 2009), with some

757   modifications.

758   For most immunocytochemistry experiments, cultured neurons were transfected at day in

759   vitro (DIV) 13 and immunostained after 72 hours. For staining, cells were fixed with 4%

760   paraformaldehyde/4% sucrose in PBS for 15 min and permeabilized in 0.2% Triton X-100

761   for 10 min at room temperature. After blocking with 10% goat serum, the cells were

762   incubated first with primary antibodies, followed by secondary antibodies. Cell surface

763   proteins were immunostained with antibodies prior to permeabilization.

764   Immunostained cells were imaged using a confocal microscopy system comprising a Nikon

765   A1 microscope with a 60x oil-immersion objective. The images were analyzed using NIS-

766   Element Software (Nikon). Except for one rabbit anti-GluA1-Ct antibody (this paper: JH4294)

767   and rabbit anti-LARGE antibody (this paper: UT1002), the following primary antibodies were

768   used for staining were obtained commercially: mouse or chicken anti-GFP (Neuromabs #75-

769   131 or Invitrogen #A10262), GluA1-Nt (Millipore), GM130 (BD Transduction Laboratories or

770   Abcam), and chicken anti-MAP2 (Covance #PCK-554P). All secondary antibodies were

771   purchased from Molecular Probes/Invitrogen/Life Technologies.

772   To quantify the confocal images presented in Figure 3C, the GluA1 intensity in the spine

773   and integrated intensity of individual endogenous GluA1 puncta in the dendritic spine were

774   measured. Images were analyzed using NIS-Elements AR (Nikon). To quantify the confocal

775   images presented in Figure 5C and 5E, fluorescence signals in the soma and dendrites were

776   quantified by measuring the area containing signals above a certain threshold. After

777   normalization, the data were statistically analyzed and plotted as a histogram. To quantify

34

778   the confocal images presented in Figure 7A–7C, we focused on the number of overlapping

779   Golgi & LARGE, Golgi & GluA1, or LARGE & GluA1 signals. These co-occurrences were

780   independent of signal intensity. Accordingly, we applied the Manders overlap coefficient,

781   which describes the degree of overlap, to the analysis of co-localization. The images were

782   acquired at a thickness of 0.6 μm. The threshold was determined using a global thresholding

783   process to separate pixels from the background, and the coefficient was calculated from the

784   pixels obtained from all slice images. Customized codes written using C++ and MATLAB

785   were used.

786

787   <u>Immunohistochemistry</u>

788   Following sacrifice, mice were transcardially perfused with solution followed by 4%

789   paraformaldehyde in PBS. The brains were quickly removed and post-fixed in the same

790   solution overnight at 4ºC. Coronal sections (50 µm thick) were cut with a vibrotome, washed

791   in PB, permeabilized in PBT. with 0.1% Triton X-100 (Sigma), and blocked with 5% heat-

792   inactivated horse serum (HS) for 1 h. The slices were then incubated with primary mouse

793   anti-GFP (1:500; Neuromab) overnight at 4ºC in PB with 5% HS. The slices were

794   subsequently washed in PB and incubated for 2 h at room temperature with an Alexa Fluor

795   488-conjugated goat anti-mouse antibody (1:1000; Invitrogen). After washing in PB, the

796   slices were mounted using Vectashield with DAPI (Vector #H1200) and stored in the dark

797   at 4ºC. High-magnification images were taken using a confocal laser-scanning microscope

798   (Nikon A1 system) equipped with lasers pretuned to 488 nm (i.e., FITC channel) and DAPI.

799   The images were analyzed using NIS-Elements AR (Nikon).

800

801   <u>Quantification and Statistical Analysis</u>

35

802 All statistical analyses were performed using SigmaPlot software (Ver 12; SYSTAT

803 Software). The statistical methods used for particular experiments are noted in the figure

804 legends. Each biological experiment was replicated at least three times using different

805 batches of cells or tissues from different animals. The number of required additional

806 experiments was determined using a power analysis, which was based on a statistical

807 analysis of the data from the first three experiments. The final data sets were analyzed using

808 a two-tailed Student's t-test for experiments with two groups and/or a one (or two)-way

809 ANOVA followed by a *post hoc* Tukey multiple comparison test for experiments with more

810 than two groups. A probability (P) value ≤0.05 was considered significant. All data points

811 were used in plots after confirming a normal distribution (data not shown). Most values are

812 presented as mean values ± standard errors of the means (SEM). Variations were calculated

813 and are presented as SEMs.

814
815
816

Acknowledgments

This work was supported by the Institute for Basic Science (IBS, R001-D1) (H-S.S.) and the University of Texas Medical Branch (UTMB) (M-G.K.). We thank Drs. Kevin P. Campbell and Richard L. Huganir for the generous gifts of cDNA plasmids, antibodies, and *Large^{myd}* mice. We thank all of the Kang Lab members for technical assistance and advice in this study.

Competing Interests

The authors declare no competing financial nor non-financial interests.

Author Contributions

M-G.K. designed and supervised the research. M-G.K. and B.A.S. wrote the paper. B.A.S., T.C., D.Z.L., H.Y.L., J-J.L. B.L., S-W.K., and M-G.K., performed experiments and analyzed the data. K.A.C., K.T.D., T.A.G., H.M.K., S-Y.C., and H-S.S contributed reagents and analytical tools and provided input and expertise.

References

Arendt, K.L., Sarti, F., and Chen, L. 2013. Chronic inactivation of a neural circuit enhances LTP by inducing silent synapse formation. *The Journal of Neuroscience 33*: 2087-2096. doi: 10.1523/JNEUROSCI.3880-12.2013

Barker, G.R., Warburton, E.C., Koder, T., Dolman, N.P., More, J.C., Aggleton, J.P., Bashir, Z.I., Auberson, Y.P., Jane, D.E., and Brown, M.W. 2006. The different effects on recognition memory of perirhinal kainate and NMDA glutamate receptor antagonism: implications for underlying plasticity mechanisms. *The Journal of Neuroscience 26*:3561-3566. doi: 10.1523/JNEUROSCI.3154-05.2006

Barnes, C.A., Jung, M.W., McNaughton, B.L., Korol, D.L., Andreasson, K., and Worley, P.F. 1994. LTP saturation and spatial learning disruption: effects of task variables and saturation levels. *The Journal of Neuroscience 14*:5793-5806.

Brockington, M., Torelli, S., Prandini, P., Boito, C., Dolatshad, N.F., Longman, C., Brown, S.C., and Muntoni, F. 2005. Localization and functional analysis of the LARGE family of glycosyltransferases: significance for muscular dystrophy. *Human Molecular Genetics 14*:657-665. doi: 10.1093/hmg/ddi062

Castro, C.A., Silbert, L.H., McNaughton, B.L., and Barnes, C.A. 1989. Recovery of spatial learning deficits after decay of electrically induced synaptic enhancement in the hippocampus. *Nature 342*:545-548. doi: 10.1038/342545a0

Cho, T., Ryu, J.K., Taghibiglou, C., Ge, Y., Chan, A.W., Liu, L., Lu, J., McLarnon, J.G., and Wang, Y.T. 2013. Long-term potentiation promotes proliferation/survival and neuronal differentiation of neural stem/progenitor cells. *PLoS One 8*:e76860. doi: 10.1371/journal.pone.0076860

Clarke, N.F., Maugenre, S., Vandebrouck, A., Urtizberea, J.A., Willer, T., Peat, R.A., Gray, F., Bouchet, C., Manya, H., Vuillaumier-Barrot, S.*, et al.* 2011. Congenital muscular dystrophy type 1D (MDC1D) due to a large intragenic insertion/deletion, involving intron 10 of the LARGE gene. *European Journal of Human Genetics 19*:452-457. doi: 10.1038/ejhg.2010.212

869 **Dillon, G.M.**, Qu, X., Marcus, J.N., and Dodart, J.C. 2008. Excitotoxic lesions restricted to
870 the dorsal CA1 field of the hippocampus impair spatial memory and extinction learning in
871 C57BL/6 mice. *Neurobiology Learning Memory 90*:426-433. doi: 10.1016/j.nlm.2008.05.008

872 **Freudenberg, F.**, Resnik, E., Kolleker, A., Celikel, T., Sprengel, R., and Seeburg, P.H. 2016.
873 Hippocampal GluA1 expression in Gria1-/- mice only partially restores spatial memory
874 performance   deficits.   *Neurobiology   Learning   Memory   135*:83-90.   doi:
875 10.1016/j.nlm.2016.07.005
876
877 **Granger, A.J.**, Shi, Y., Lu, W., Cerpas, M., and Nicoll, R.A. 2012. LTP requires a reserve
878 pool of glutamate receptors independent of subunit type. *Nature 493*:495-500. doi:
879 10.1038/nature11775

880 **Guitar, N.A.**, and Roberts, W.A. 2015. The interaction between working and reference
881 spatial memories in rats on a radial maze. *Behavioural Processes 112*:100-107. doi:
882 10.1016/j.beproc.2014.10.007
883

884 **Hall, R.A.**, Hansen, A., Andersen, P.H., and Soderling, T.R. 1997. Surface expression of
885 the AMPA receptor subunits GluR1, GluR2, and GluR4 in stably transfected baby hamster
886 kidney cells. *Journal of Neurochemistry 68*:625-630.

887 **Hanley, J.G.** 2010. Endosomal sorting of AMPA receptors in hippocampal neurons.
888 *Biochemical Society Transactions 38*:460-465. doi: 10.1042/BST0380460

889 **Hernandez, C.M.**, Kayed, R., Zheng, H., Sweatt, J.D., and Dineley, K.T. (2010). Loss of
890 alpha7 nicotinic receptors enhances beta-amyloid oligomer accumulation, exacerbating
891 early-stage cognitive decline and septohippocampal pathology in a mouse model of
892 Alzheimer's   disease.   *The   Journal   of   Neuroscience   30*:2442-2453.   doi:
893 10.1523/JNEUROSCI.5038-09.2010

894 **Holzfeind, P.J.**, Grewal, P.K., Reitsamer, H.A., Kechvar, J., Lassmann, H., Hoeger, H.,
895 Hewitt, J.E., and Bittner, R.E. 2002. Skeletal, cardiac and tongue muscle pathology,
896 defective retinal transmission, and neuronal migration defects in the Large(myd) mouse
897 defines a natural model for glycosylation-deficient muscle - eye - brain disorders. Human
898 Molecular Genetics *11*:2673-2687.

899 **Huganir, R.L.**, and Nicoll, R.A. 2013. AMPARs and synaptic plasticity: the last 25 years.
900 *Neuron 80*:704-717. doi: 10.1016/j.neuron.2013.10.025

901 **Kanagawa, M.**, Saito, F., Kunz, S., Yoshida-Moriguchi, T., Barresi, R., Kobayashi, Y.M.,
902 Muschler, J., Dumanski, J.P., Michele, D.E., Oldstone, M.B*., et al.* 2004. Molecular
903 recognition by LARGE is essential for expression of functional dystroglycan. *Cell 117*:953-
904 964. doi: 10.1016/j.cell.2004.06.003

905   **Kang, M.G.**, Guo, Y., and Huganir, R.L. 2009. AMPA receptor and GEF-H1/Lfc complex
906   regulates dendritic spine development through RhoA signaling cascade. *Proceedings of the*
907   *National Academy of Sciences 106*:3549-3554. doi: 10.1073/pnas.0812861106

908   **Kang, M.G.**, Nuriya, M., Guo, Y., Martindale, K.D., Lee, D.Z., and Huganir, R.L. 2012.
909   Proteomic Analysis of alpha-Amino-3-hydroxy-5-methyl-4-isoxazole Propionate Receptor
910   Complexes. *The Journal Biological Chemistry 287*:28632-28645. doi:
911   10.1074/jbc.M111.336644

912   **Lee, D.Z.**, Chung, J.M., Chung, K., and Kang, M.G. 2012. Reactive oxygen species (ROS)
913   modulate AMPA receptor phosphorylation and cell-surface localization in concert with pain-
914   related behavior. *Pain 153*:1905-1915. doi: 10.1016/j.pain.2012.06.001

915   **Levi, S.**, Grady, R.M., Henry, M.D., Campbell, K.P., Sanes, J.R., and Craig, A.M. (2002).
916   Dystroglycan is selectively associated with inhibitory GABAergic synapses but is
917   dispensable for their differentiation. *The Journal of Neuroscience 22*:4274-4285. doi:
918   20026440

919   **Lisi, M.T.**, and Cohn, R.D. 2007. Congenital muscular dystrophies: new aspects of an
920   expanding group of disorders. *Biochimica et Biophysica Acta 1772*:159-172. doi:
921   10.1016/j.bbadis.2006.09.006

922   **Longman, C.**, Brockington, M., Torelli, S., Jimenez-Mallebrera, C., Kennedy, C., Khalil, N.,
923   Feng, L., Saran, R.K., Voit, T., Merlini, L.*, et al.* (2003). Mutations in the human LARGE gene
924   cause MDC1D, a novel form of congenital muscular dystrophy with severe mental
925   retardation and abnormal glycosylation of alpha-dystroglycan. *Human Molecular Genetics*
926   *12*:2853-2861. doi: 10.1093/hmg/ddg307

927   **Lynch, M.A.** 2004. Long-term potentiation and memory. *Physiological Reviews 84*:87-136.
928   doi: 10.1152/physrev.00014.2003

929   **McNaughton, B.L.**, Barnes, C.A., Rao, G., Baldwin, J., and Rasmussen, M. 1986. Long-
930   term enhancement of hippocampal synaptic transmission and the acquisition of spatial
931   information. *The Journal of Neuroscience 6*:563-571.

932   **Michele, D.E.**, Barresi, R., Kanagawa, M., Saito, F., Cohn, R.D., Satz, J.S., Dollar, J.,
933   Nishino, I., Kelley, R.I., Somer, H.*, et al.* 2002. Post-translational disruption of dystroglycan-
934   ligand interactions in congenital muscular dystrophies. *Nature 418*:417-422. doi:
935   10.1038/nature00837

936   **Nabavi, S.**, Fox, R., Proulx, C.D., Lin, J.Y., Tsien, R.Y., and Malinow, R. 2014. Engineering
937   a memory with LTD and LTP. *Nature 511*:348-352. doi: 10.1038/nature13294

40

938 **Okajima, T.**, Xu, A., Lei, L., and Irvine, K.D. 2005. Chaperone activity of protein O-
939 fucosyltransferase 1 promotes notch receptor folding. *Science 307*:1599-1603. doi:
940 10.1126/science.1108995

941 **Peyrard, M.**, Seroussi, E., Sandberg-Nordqvist, A.C., Xie, Y.G., Han, F.Y., Fransson, I.,
942 Collins, J., Dunham, I., Kost-Alimova, M., Imreh, S.*, et al.* 1999. The human LARGE gene
943 from 22q12.3-q13.1 is a new, distinct member of the glycosyltransferase gene family.
944 *Proceedings of the National Academy of Sciences 96*:598-603.

945 **Pribiag, H.**, Peng, H., Shah, W.A., Stellwagen, D., and Carbonetto, S. (2014). Dystroglycan
946 mediates homeostatic synaptic plasticity at GABAergic synapses. *Proceedings of the*
947 *National Academy of Sciences 111*:6810-6815. doi: 10.1073/pnas.1321774111

948 **Sanders, M.J.**, Wiltgen, B.J., and Fanselow, M.S. 2003. The place of the hippocampus in
949 fear conditioning. European Journal Pharmacology *463*:217-223.

950 **Sanderson, D.J.**, Good, M.A., Skelton, K., Sprengel, R., Seeburg, P.H., Rawlins, J.N., and
951 Bannerman, D.M. 2009. Enhanced long-term and impaired short-term spatial memory in
952 GluA1 AMPA receptor subunit knockout mice: evidence for a dual-process memory model.
953 *Learning & Memory 16*:379-386. doi: 10.1101/lm.1339109

954 **Satz, J.S.**, Ostendorf, A.P., Hou, S., Turner, A., Kusano, H., Lee, J.C., Turk, R., Nguyen, H.,
955 Ross-Barta, S.E., Westra, S.*, et al.* 2010. Distinct functions of glial and neuronal
956 dystroglycan in the developing and adult mouse brain. *The Journal of Neuroscience*
957 *30*:14560-14572. doi: 10.1523/JNEUROSCI.3247-10.2010

958 **Soares, C.**, Lee, K.F., Nassrallah, W., and Beique, J.C. (2013). Differential subcellular
959 targeting of glutamate receptor subtypes during homeostatic synaptic plasticity. *The Journal*
960 *of Neuroscience 33*:13547-13559. doi: 10.1523/JNEUROSCI.1873-13.2013

961 **Spear, N.E.**, and Miller, R.R. 1981. Information processing in animals, memory mechanisms
962 (Hillsdale, N.J.: L. Erlbaum Associates).

963 **Stilling, R.M.**, Benito, E., Gertig, M., Barth, J., Capece, V., Burkhardt, S., Bonn, S., and
964 Fischer, A. 2014. De-regulation of gene expression and alternative splicing affects distinct
965 cellular pathways in the aging hippocampus. *Frontiers in Cellular Neuroscience 8*:373. doi:
966 10.3389/fncel.2014.00373

967 **Tomita, S.**, Chen, L., Kawasaki, Y., Petralia, R.S., Wenthold, R.J., Nicoll, R.A., and Bredt,
968 D.S. 2003. Functional studies and distribution define a family of transmembrane AMPA
969 receptor regulatory proteins. *The Journal of Cell Biology 161*:805-816. doi:
970 10.1083/jcb.200212116

971 **Traunmuller, L.**, Gomez, A.M., Nguyen, T.M., and Scheiffele, P. 2016. Control of neuronal
972 synapse specification by a highly dedicated alternative splicing program. *Science 352*:982-
973 986. doi: 10.1126/science.aaf2397

974 **Turrigiano, G.G.** 2008. The self-tuning neuron: synaptic scaling of excitatory synapses. *Cell*
975 *135*:422-435. doi: 10.1016/j.cell.2008.10.008

976 **Vaillend, C.**, Poirier, R., and Laroche, S. 2008. Genes, plasticity and mental retardation.
977 *Behavioural Brain Research 192*:88-105. doi: 10.1016/j.bbr.2008.01.009

978 **von Engelhardt, J.**, Mack, V., Sprengel, R., Kavenstock, N., Li, K.W., Stern-Bach, Y., Smit,
979 A.B., Seeburg, P.H., and Monyer, H. 2010. CKAMP44: a brain-specific protein attenuating
980 short-term synaptic plasticity in the dentate gyrus. *Science 327*:1518-1522. doi:
981 10.1126/science.1184178
982
983
984

Figure Legends

Figure 1 LARGE is necessary for neuronal homeostatic scaling-down (**A**) Total LARGE expression increased significantly during synaptic scaling-down in response to a 2-day bicuculline treatment (Bicu), but was not significantly affected by 2-day tetradotoxin (TTX)-induced synaptic scaling-up. Our surface biotinylation approach (schema) revealed increased and decreased surface GluA1 expression levels in response to treatment with TTX and Bicu, respectively, which confirmed the respective induction of scaling-up and -down (n = 4; two-tailed t-test, *P <0.01, **P <0.001). (**B**) During synaptic scaling-down, inverse correlations of LARGE expression were observed with surface GluA1 and GluA2 expression (n = 6; one-way ANOVA, *P <0.05, **P <0.005). The decrease of surface GluA1 was greater than that of GluA2 (n = 6; two-way RM ANOVA, #P <0.001). (**C**) High-density hippocampal cultures were infected with an AAV expressing scrambled shRNA with GFP (Cont), *LARGE* shRNA with GFP (shRNA) or *LARGE* rescue (Rescue). At DIV (Day of *in vitro*) 14, the neurons were subjected to surface biotinylation after a 2-day Bicu or TTX treatment. The Bicu-induced decrease in surface GluA1 expression was blocked by the knockdown (KD) of endogenous LARGE with *LARGE* shRNA (shRNA), but reversed by *LARGE* rescue (Rescue) (n = 4; one-way ANOVA, *P <0.05, **P <0.005). (**D**) The Bicu-induced decrease in mEPSC amplitude was blocked by the shRNA-mediated knockdown (KD) of endogenous *LARGE*, but was reversed by *LARGE* rescue (Rescue) (1300, 1300, 1300, and 1262 events from n = 17, 16, 15, and 13 neurons, respectively; one-way ANOVA; amplitude, $F_{(3,57)}$ =15.558, *P <0.005, **P <0.001; frequency; $F_{(3,57)}$ =0.619, P =0.606). Representative images show GFP-positive and negative neurons in a whole-cell patch clamp experiment. Cultured hippocampal neurons transfected on DIV (Day of *in vitro*) 8 with cDNA plasmids expressing either scrambled shRNA with GFP, *LARGE* shRNA with GFP,

43

1010   or *LARGE* shRNA with GFP and LARGE rescue with GFP, were subjected to a whole-cell

1011   patch clamp experiment after a 2-day treatment with Bicu or TTX. A calcium phosphate

1012   method was used to yield a transfection efficiency of approximately 20%. Scale bar = 10 µm.

1013

1014   **Figure 2** LARGE downregulates the surface localization of AMPA-R. (**A**) *LARGE*

1015   knockdown (KD) increased cell-surface GluA1 (Surface) expression, which was reversed by

1016   *LARGE* rescue. However, changes in LARGE expression did not affect the total GluA1

1017   (Input) or GluN1 expression (n = 3; one-way ANOVA, *P <0.001, **P <0.005, ***P <0.05).

1018   (**B**) A schema of the *ex vivo* cross-linking of surface proteins using BS^3. Cross-linked and

1019   non-cross-linked proteins are indicated by high-molecular-weight (Surface) and low-

1020   molecular-weight bands (Internal), respectively. Surface GluA1 levels increased and internal

1021   GluA1 levels decreased in homozygous (-/-) mice (Large^{myd}) *ex vivo,* compared with wild-

1022   type (+/+) and heterozygous (+/-) mice. GluN2B was used as an internal control (n = 3; two-

1023   tailed t-test, *P <0.001, **P <0.05). (**C**) An imaging analysis of cultured neurons revealed

1024   higher levels of surface-localized GluA1 (sGluA1) in neurons expressing *LARGE* shRNA

1025   (GFP-positive neurons) than in neighboring GFP-negative neurons (Cont). The GluA1

1026   antibody was applied before neuron permeabilization. MAP2, a marker of neuronal dendrites,

1027   was used to determine the number and morphology of neurons (n = 20, 20 neurons; Mann–

1028   Whitney rank-sum test, T = 234, U = 24, *P <0.001). Scale bars = 10 µm. (**D**) Co-expression

1029   of LARGE-GFP (LARGE or LRG) with myc-GluA1 (GluA1) and myc-GluA2 (GluA2) in

1030   HEK293T cells significantly reduced the respective cell-surface localization of GluA1

1031   (sGluA1) and GluA2 (sGluA2). However, total GluA1 (tGluA1) and GluA2 (tGluA2) levels in

1032   the Input were not significantly altered (n = 8; two-tailed t-test, *P <0.001). (**E**) Co-expression

44

1033   of LARGE with GFP-GluA1 significantly reduced cell-surface GluA1 (sGluA1) levels at

1034   cultured neurons. A schema of our imaging assay. sGluA1 was labeled with a red

1035   fluorophore-conjugated anti-GluA1 antibody prior to neuron permeabilization. After

1036   permeabilization, total GluA1 (tGluA1) was stained using a green fluorophore-conjugated

1037   anti-GFP antibody (n = 10, 10 neurons; Mann–Whitney rank-sum test, T = 147, U = 8, *P

1038   <0.005). Scale bar = 10 μm.

1039

1040   **Figure 3** LARGE directly interacted with AMPA-R to increase AMPA-R localization at the

1041   Golgi. (**A**) Confocal images demonstrating major pools of GFP-tagged LARGE (LARGE-

1042   GFP) in the cis-Golgi (Top), trans-Golgi (middle), and Golgi outposts (bottom) of cultured

1043   hippocampal neurons. GM130 and TGN38 are cis-Golgi and trans-Golgi marker proteins,

1044   respectively. Scale bar = 10 μm. (**B**) *LARGE* knockdown (KD; shRNA) decreased the

1045   number of GluA1 molecules at the Golgi, compared with non-transfected and scrambled-

1046   shRNA transfected neurons (Cont). This phenomenon was reversed by *LARGE* rescue

1047   (Rescue) (n = 12, 11, 12, 13 neurons; $F_{(2,33)}$ = 31.618, *P <0.001, **P <0.002). Scale bar =

1048   30 μm. (**C**) The density gradient-based subcellular fractionation of HEK293T cells revealed

1049   that the co-expression of LARGE with GluA1 (+LRG) significantly altered the distribution of

1050   AMPA-R pools in the Golgi and plasma membrane. In the +LRG group, the relative size of

1051   the GluA1 pool at the Golgi (GM130) increased significantly whereas that in the plasma

1052   membrane (P-Cadherin) decreased significantly relative to the control group (-LRG, GluA1

1053   only) (n = 3; two-tailed t-test, *P <0.05). (**D**) Subcellular fractionation of hippocampal tissues

1054   from *Large* knockout mice (*Large*myd-/-) revealed relative decreases and increases,

1055   respectively, in the relative sizes of the GluA1 pools in the Golgi and plasma membrane,

1056   compared with those in wild-type mice (WT) (n = 3, 3 mice; two-tailed t-test, *P <0.05, **P

45

1057 <0.001). (**E**) Heterologous HEK293T cells in which LARGE-GFP had been co-expressed

1058 with myc-tagged GluA1 (myc-GluA1) were subjected to immunoprecipitation (IP). IP of

1059 LARGE with an anti-GFP antibody specifically co-immunoprecipitated GluA1 (left), and IP

1060 of GluA1 with an anti-myc antibody specifically co-immunoprecipitated LARGE (right). (**F**)

1061 The direct interaction between LARGE and AMPA-R was examined using an enzyme-linked

1062 immunosorbent assay (ELISA). The LARGE ectodomain (Catalytic domain 1 [CD1] + CD2)

1063 used to coat the bottom of the plate bound directly to the Fc-fused N-terminal ectodomain

1064 of GluA1 (GluA1-Fc). Binding was quantified by measuring the activity of FC antibody-

1065 coupled peroxidase (n = 3; $F_{(5,12)}$ = 293.046, *P <0.001, **P <0.01). (**G**) Another ELISA used

1066 to evaluate the relative binding affinities of LARGE for each AMPA-R subunit yielded the

1067 following order from highest to lowest: GluA1 > GluA2 > GluA4 (n = 3; $F_{(2,12)}$ = 867.644, *P

1068 <0.001 compared with GluA2 and GluA4). (**B**, **F**) One-way ANOVA, (**G**) two-way RM ANOVA.

1069

1070 **Figure 4** The LARGE-associated pool of AMPA-R at the Golgi increases during homeostatic

1071 scaling-down. (**A-C**) A series of confocal microscopy images of cultured hippocampal

1072 neurons double-stained for a Golgi marker (GM130) and LARGE or GluA1 yielded several

1073 findings. (**A**) LARGE localization at the Golgi increased significantly after a 48-h bicuculline

1074 treatment (Bicu 48h) (n = 9, 10 neurons; two-tailed t-test, t_{17} = -3.937, *P <0.001). Scale bar

1075 = 10 μm. (**B**) GluA1 localization at the Golgi increased significantly in response to Bicu 48h

1076 (n = 12, 13 neurons; Mann–Whitney rank-sum test, T = 90, U = 12, *P <0.001). (**C**) The co-

1077 localization of GluA1 and LARGE in the perinuclear region increased significantly in

1078 response to Bicu 48h (n = 9, 10 neurons; two-tailed t-test, t_{17} = -4.728, *P <0.001). (**D**)

1079 Density gradient fractionation of subcellular organelles revealed significant increases in the

1080 relative amounts of GluA1 and LARGE in the Golgi fraction following treatment with Bicu

1081   48h (n = 4; two-tailed t-test, *P <0.05, **P <0.005). (**E**) Bicu 48h significantly increased the

1082   binding of LARGE to GluA1, as demonstrated by the increased co-immunoprecipitation of

1083   LARGE and GluA1 (n = 3; two-tailed t-test, *P <0.01). (**F**) Schema of our working model for

1084   the regulation of AMPA-R trafficking by LARGE during homeostatic scaling-down.

1085

1086   **Figure 5** *LARGE* knockdown (KD) causes synaptic AMPA-R overload and thus impairs long-

1087   term potentiation (LTP) in the hippocampal CA1 region. (**A**) A schema, plot, and traces from

1088   an *in vivo* LTP analysis after an injection of virus encoding *LARGE* shRNA. *LARGE* KD (LRG

1089   shRNA) was found to impair LTP (n = 8, 8 mice; two-tailed t-test, *P <0.05). Scale bar = 300

1090   μm. (**B**) Whole-cell patch clamping yielded current traces, cumulative plots, and scattered

1091   plots from an mEPSC analysis following transfection with plasmids encoding scrambled

1092   shRNA (Cont), *LARGE* shRNA, or *LARGE* rescue. *LARGE* KD increased the amplitude but

1093   not the frequency of mEPSC, whereas *LARGE* rescue reversed this amplitude change.

1094   Three different groups from 48 coverslips in four batches of neuronal culture were recorded

1095   (n = 1653, 1660, and 1622 events from *n* = 17, 17, and 17 neurons, respectively; Amplitude,

1096 $F_{(2,48)}$ = 17.815, *P <0.001, **P = 0.026; Frequency, $F_{(2,48)}$ = 0.452, P = 0.639; Cont: black,

1097   shRNA: red, Rescue: cyan). (**C**) *LARGE* KD (shRNA) increased the number of GluA1

1098   molecules in the dendritic spines, whereas this phenomenon was reversed by *LARGE*

1099   rescue (n = 529, 529, and 562 spines from *n* = 13, 14, and 14 neurons, respectively; $F_{(2,38)}$

1100   = 25.026, *P <0.001, **P <0.005). Scale bars = 30 μm (whole cell image) and 10 μm

1101   (dendrite). (**D**) Schema, blot, and bar graph of a western blot analysis of GluA1 expression

1102   in the postsynaptic density (PSD) of hippocampi from *LARGE* knockout (KO) mice (-/-),

1103   demonstrating increased synaptic AMPA-R expression relative to that observed in WT mice

1104   (+/+) *in vivo* (*n* = 3, 3 mice; two-tailed t-test, *P <0.005). (b, c) one-way ANOVA.

47

1105

1106   **Figure 6** LARGE deficiency impairs fear memory. (**A**) Schema of a fear memory test. (**B**)

1107   *LARGE* knockout (KO) did not induce differences in fear conditioning (n = 7, 7, 7 mice) (**C**,

1108   **D**) Contextual and cued fear memory deficits were observed in KO mice (-/-). (*n* = 7, 7, 7

1109   mice; contextual, $F_{(2,18)}$ = 6.808, *P <0.01; cued, $F_{(2,18)}$ = 12.148, **P <0.001). (**E**) No

1110   differences in fear conditioning were observed in *LARGE* knockdown (KD) mice (*n* = 19, 19

1111   mice). (**F**) Contextual memory deficits were observed in *LARGE* KD mice (*n* = 19, 19 mice,

1112   two-tailed t-test, t_{36} = 3.684, *P <0.01). (**G**) No differences were observed in cued memory

1113   (*n* = 19, 19 mice, Mann–Whitney rank-sum test, T = 390, U = 161, *P* = 0.579). (**H**) No

1114   differences in fear conditioning were observed in *LARGE* KD rats (*n* = 9, 10 mice). (**I**)

1115   Contextual memory deficits were observed in *LARGE* KD rats (*n* = 9, 10 rats, two-tailed t-

1116   test, t_{17} = 5.709, *P <0.005). (**J**) No differences were observed in cued memory (*n* = 9, 10

1117   mice, two-tailed t-test, t_{17} = -0.0162, *P* = 0.987). (**E**–**J**) Animals were injected with a virus

1118   expressing either scrambled (Cont) or *LARGE* shRNA with GFP (shRNA). (**B**, **E**, **H**) Two-

1119   way RM ANOVA, (**C**, **D**) One-way ANOVA.

1120

1121   **Figure 7** LARGE deficiency impairs hippocampus-dependent long-term but not short-term

1122   memory. (**A**) In the open field test, no differences were observed in the distances moved

1123   and time spent in the center (*n* = 16, 16 mice; center time, two-tailed t-test, t_{30} = 1.393, *P* =

1124   0.174). (**B**) In the Y-maze-based working memory test, no differences were observed in

1125   spontaneous alternations or the total number of entries (*n* = 16, 16 mice, two-tailed t-test, t_{30}

1126   = 0.581, *P* = 0.566). (**C**) In the simple novelty preference test, *LARGE* knockdown (KD) mice

1127   exhibited a preference in the short term (1 min; n = 12, 12 mice, Mann–Whitney rank-sum

1128   test; entries, T = 168, U = 54, *P* = 0.308; time, T = 141, U = 57, *P* = 0.601), but not in the

48

1129   long term (24 h; n = 12, 12 mice, two-tailed t-test; entries, t_{22} = 2.727, *P = 0.012; time, t_{22} =

1130   2.483, **P = 0.021). ITI: inter-trial intervals. The novel arm preference was calculated as

1131   (novel/novel + other) x 100%. (**D**) In the novel object recognition test, control and *LARGE*

1132   KD mice similarly explored two identical objects during training (n = 19, 20 mice, two-tailed

1133   t-test, t_{37} = 0.556, P = 0.582). Both groups exhibited similar preferences during a short-term

1134   memory test (5 min; n = 19, 20 mice, Mann–Whitney rank-sum test, T = 393, U = 177, P =

1135   0.725). In a long-term memory test, *LARGE* KD mice exhibited no preference for the novel

1136   object (24 h; n = 19, 20 mice, two-tailed t-test, t_{37} = 3.773, *P <0.001). The novel object

1137   preference was calculated as (novel/novel + familiar) x 100%. (**A**) Two-way RM ANOVA for

1138   distance moved.

1139

1140   **Figure 1-figure supplementary 1.** Validation of AAV expressing *LARGE* shRNA

1141   with GFP. (**A**) A representative fluorescence image of GFP signals demonstrated

1142   that most cultured hippocampal neurons were infected by the AAV. (**B**) Differential

1143   interference contrast (DIC) image shows the number and shape of neurons in the

1144   culture. These live images were recorded with 20x objective attached to a Nikon

1145   TMD inverted microscope system connected to a Nikon digital camera system

1146   (Digital-Sight DS-2Mv). (**C**) Western blot analysis confirmed knockdown of *LARGE*.

1147   Scrambled shRNA was used as control (Cont) (n=3, two tailed t-test, *P < 0.005).

1148   Scale bar = 100 μm.

1149

1150   **Figure 1-figure supplementary 2.** LARGE is necessary for neuronal homeostatic

1151   scaling-down but not for scaling-up. (**A**) Confocal images of cultured hippocampal

49

1152   neurons confirmed the increase in LARGE expression in response to Bicu but not

1153   TTX (n = 13, 13, 13 neurons; Mann–Whitney rank sum test, T = 91, U = 0, *P <0.001;

1154   Blue: DAPI, red: endogenous LARGE). Scale bar = 10 μm. (**B**) The TTX-induced

1155   increase in surface GluA1 was not affected by LARGE shRNA or LARGE rescue. (n

1156   = 3; one-way ANOVA, *P <0.001, **P = 0.027). (**C**) The TTX-induced increase in

1157   mEPSC amplitude was not affected by LARGE KD or rescue (1300, 1270, 1300, and

1158   1279 events from n = 17, 13, 14, and 13 neurons, respectively; one-way ANOVA;

1159   amplitude, $F_{(3,53)}$ =7.783, *P <0.001; frequency; $F_{(3,53)}$ =1.211, P = 0.315). The

1160   mEPSC traces and cumulative and scattered plots are shown. Nine different groups

1161   were recorded using 60 coverslips from three batches of neuronal culture.

1162

1163   **Figure 1-figure supplementary 3.** Verification of low-level batch-to-batch variation

1164   in our mEPSC experiments. (**A**) The amplitude and frequency did not vary among

1165   the batches used in experiments (**B**) The amplitude and frequency did not vary

1166   between non-transfected and GFP-transfected neurons

1167

1168   **Figure 3-figure supplementary 1.** LARGE increased AMPA-R pool in the Golgi. (**A**)

1169   GFP-GluA1 in Golgi was increased by LARGE overexpression (GluA1 + LRG),

1170   compared with a control (GluA1) (n = 30, 30 cells; Two tailed t-test, *P < 0.001). Co-

1171   localization of GluA1 with GM130 in HEK293T cells analyzed by 3D reconstruction

1172   of a series of z-stack confocal images. Complete (yellow) and partial co-localization

1173   (orange). Co-localization of GluA1 and LARGE was quantified using the co-

1174   localization analysis tool in the NIS-Elements software (Nikon). In the analysis,

1175   Manders overlap coefficients were given and used to obtain the relative co-

1176   localization values between those two proteins. Scale bar = 10 µm. (**B**) Fractionation

1177   of subcellular organelles from the hippocampal CA1 of mice. Representative data

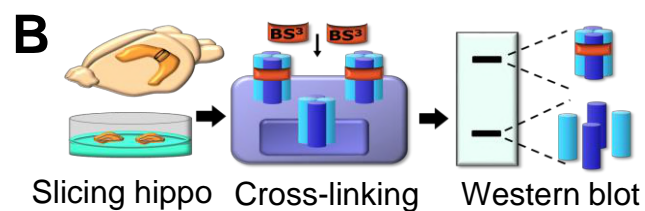1178   showing the fractionation of organelle markers and LARGE. P-cadherin, plasma

1179   membrane marker; GM130, Golgi markers.

1180

1181   **Figure 3–figure supplementary 2.** LARGE directly interacts with AMPA-R subunits.

1182   (**A**) LARGE interacted with GluA2 inside of cell (lower band) but not with GluA2 at

1183   the plasma membrane (upper band). Analysis of LARGE association with AMPA-R

1184   determined by immunoprecipitation (IP). HEK293T cells were transfected with myc-

1185   GluA1, myc-GluA2, and/or LARGE-GFP. IP with anti-GFP antibody. Both GluA1 and

1186   GluA2 were co-immunoprecipitated with LARGE-GFP. As see in Input, GluA2 yield

1187   two bands (upper and lower bands). Most GluA2 co-immunoprecipitated with

1188   LARGE was GluA2 correspond to intracellular GluA2, judging from its molecular

1189   weight. (**B**-**E**) Purification of GluA1 and LARGE (catalytic domain 1 [CD1] + CD2)

1190   proteins. SDS-PAGE (**B**) and Western-blot (**C**) analysis of purified GluA1Nt-Fc fusion

1191   protein. SDS-PAGE (**D**) and Western-blot (**E**) analysis of purified LARGE.

1192

1193   **Figure 3–figure supplementary 3.** LARGE interaction with AMPA-R did not change

1194   glycosylation of AMPA-R. No change in N- and O-glycosylation of GluA1 with co-

1195   expression of LARGE in HEK293T cells. N-linked glycosylation of GluA1 was

1196 analyzed using two de-glycosylation enzymes, endoglycosidase F (Endo-F) and

1197 endoglycosidase H (Endo-H). Endo-F completely de-glycosylated all GluA1

1198 regardless of LARGE co-expression, and there was no difference in the amount of

1199 Endo-H–sensitive and –insensitive forms of GluA1 with co-expression of LARGE. In

1200 addition to N-linked glycosylation of GluA1, O-linked glycosylation of GluA1 was

1201 analyzed using O-glycosidase (O-Gly). The size of a GluA1 band was not changed

1202 by O-Gly treatment, suggesting that GluA1 does not have O-glycosylation. Co-

1203 expression of LARGE did not changed the O-glycosylation status of GluA1. Method:

1204 In HEK293T cells, myc-GluA1 and LARGE were expressed by transfection of their

1205 plasmids. From the lysate of the cells, myc-GluA1 was immunoprecipitated and

1206 treated with Endo-F (500 unit) and Endo H (500 unit) at 37℃ for 2 hours, or with O-

1207 Gly (50000 unit) followed with SDS-PAGE and Western blot analyses.

1208

1209 **Figure 5-figure Supplementary 1.** Electrophysiological analyses after knockdown

1210 of *LARGE* at CA1 of hippocampus. (**A**) AMPA-R fEPSP amplitudes were significantly

1211 increased by LARGE KD. Input-output curves shown relating stimulus strength to

1212 fEPSPs (output amplitude), which is greater in a LRG shRNA group (n = 5, 5 mice;

1213 Two-way repeated-measures ANOVA with post hoc Bonferroni t-test, *P < 0.05, **P

1214 < 0.001). (**B**) Intact short-term plasticity. Mean PPR (FP2/FP1) of fEPSPs plotted as

1215 a function of inter-pulse. Field potential (FP) data are mean ± s.e.m. (group: P =

1216 0.565, group x interval: P = 0.170, n=5, 5). (**C**) LARGE did not affect inhibitory

1217 synaptic strength. mIPSC recordings from Cont, shRNA, and Rescue. No significant

1218   differences in mIPSC amplitude and frequency were observed among the groups.

1219   Three different groups were recorded using 27 coverslips in 3 batches of neuronal

1220   culture (1098, 1080, 1055 events from n = 12, n=12, n=11 neurons, respectively;

1221   Amplitude, $F_{(2,32)}$=0.553, P =0.58; Frequency, $F_{(2,32)}$=0.292, P=0.749). Scale bar =

1222   30 μm.

1223

1224   **Figure 5-figure supplementary 2.** Confocal image analyses demonstrated the

1225   effect of *LARGE* KD on structural synaptic plasticity. Confocal images of cultured

1226   hippocampal neurons showed that *LARGE* KD (shRNA) significantly increase not

1227   the number of spines but the size of spines compared to that of control neurons,

1228   which was reversed by LARGE rescue (*n* = 7, 7, 7 neurons; One-way ANOVA, *P <

1229   0.01, **P < 0.005). In the cultured hippocampal neurons, neuronal dendrites and

1230   spines was visualized by GFP. PSD95 is synaptic marker. MAP2 is dendrite marker.

1231   Scale bar = 10μm.

1232

1233   **Figure 6-figure supplementary 1** Confirmation of knockdown efficiency of LARGE

1234   shRNA after *in vivo* electrophysiology analyses and behavior tests. (**A**)

1235   Immunohistochemistry and RT-PCR analysis of mouse hippocampal CA1 region

1236   infected with AAV. Confocal images showed the location and diffusion range of AAV

1237   microinjected into CA1. Endogenous *LARGE* mRNA expression in CA1 was

1238   significantly knocked down by infection of AAV expressing *LARGE* shRNA with GFP

1239   (shRNA) (n = 3, 3 mice; Two tailed t-test, *P < 0.001). Scale bar = 100 μm (left), 50

53

1240 µm (right). (**B**) Digital image and Western blot analysis of hippocampal CA1 region

1241 of rat brain infected with AAV. Brain slices were imaged by digital imaging under a

1242 blue LED light. Strong and specific expression of GFP in hippocampi indicated

1243 specific delivery and expression of *LARGE* shRNA with GFP by AAV injection.

1244 Western blot analyses confirmed knockdown of *LARGE* in GFP-expressing

1245 hippocampi (n = 3, 3 rats; Two tailed t-test, *P < 0.005)

1246

1247 **Figure 6-figure supplementary 2** The absence of a significant difference in shock

1248 threshold among groups demonstrated that LARGE expression status did not affect

1249 fear conditioning. (**A**) Schema of shock threshold tests of animals. Shocks (gray

1250 blocks) were delivered every 30 s, with intensity increasing from 0.1 mA to 1.0 mA

1251 (4:28, 4:58) and decreasing back to 0.1 mA (10:30). (**B**) Regardless of genotype or

1252 injected AAV, all animals responded to shocks in a similar way. The shock intensity

1253 thresholds for jumping, vocalization, and flinching were measured for wild type (+/+),

1254 heterozygous (+/-), and knockout (-/-) animals and animals injected with AAV

1255 expressing scrambled shRNA with GFP (Cont) or *LARGE* shRNA with GFP (shRNA).
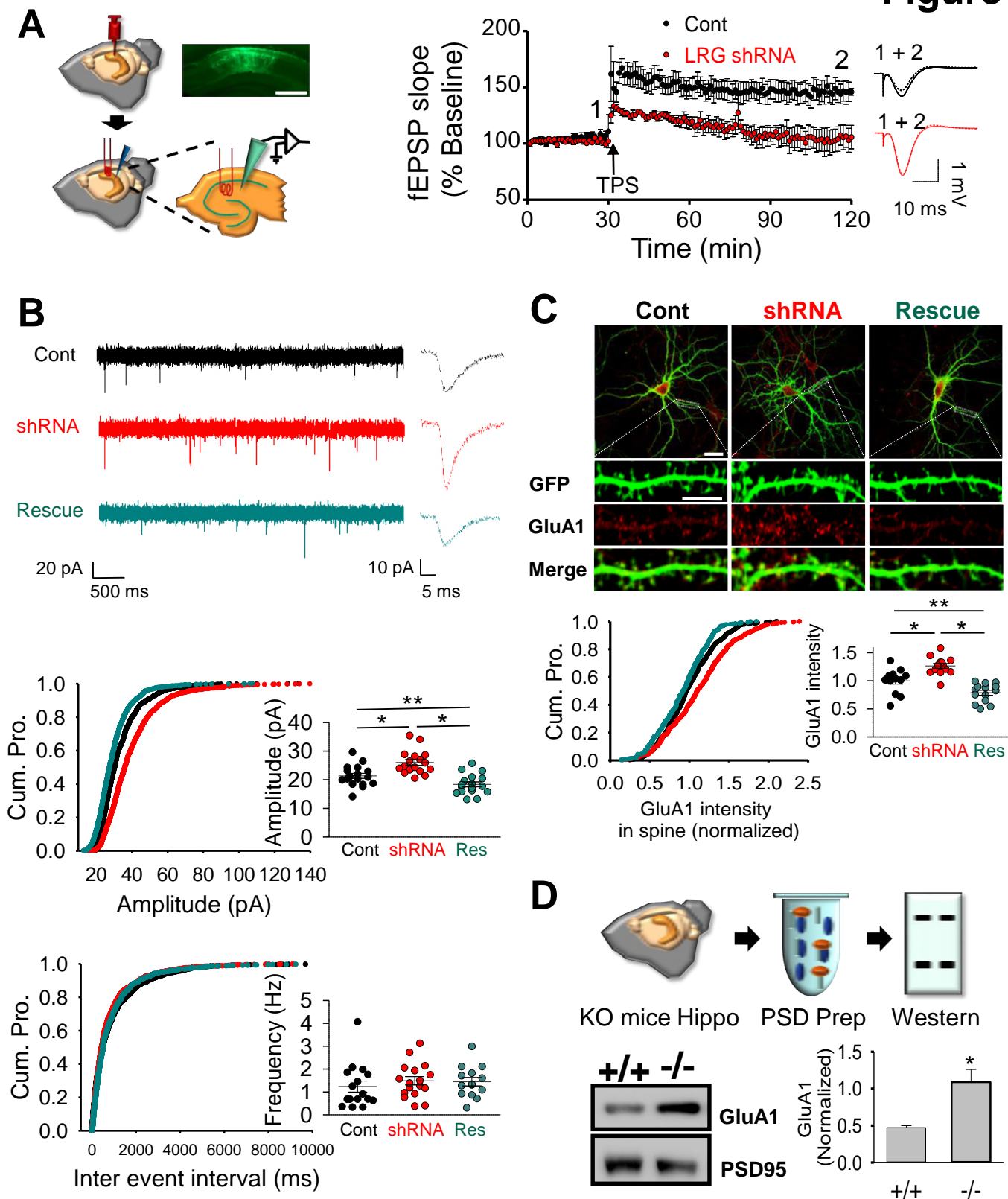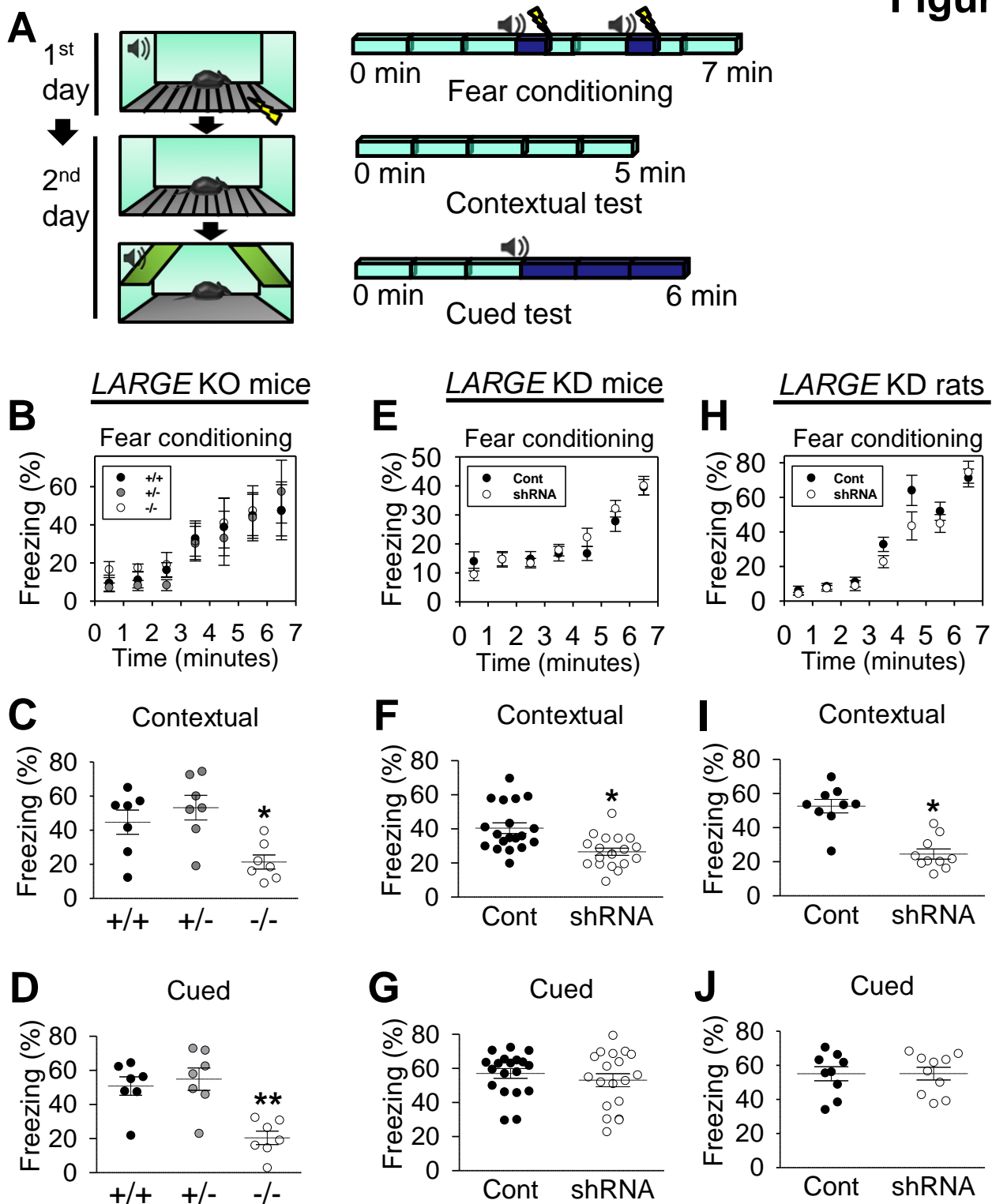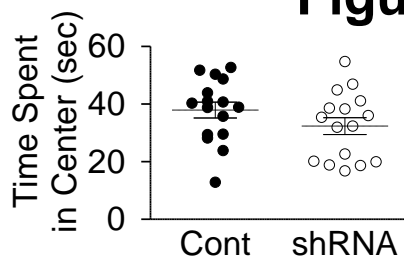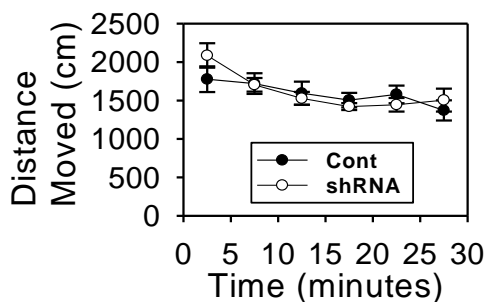
1256

Figure 1

Figure 2

Figure 3

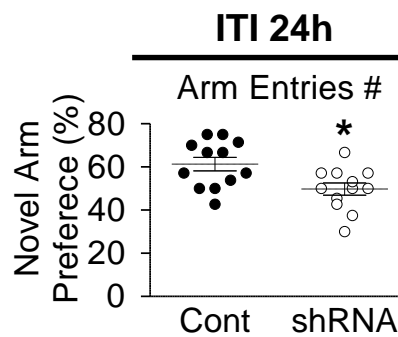**Figure 4**
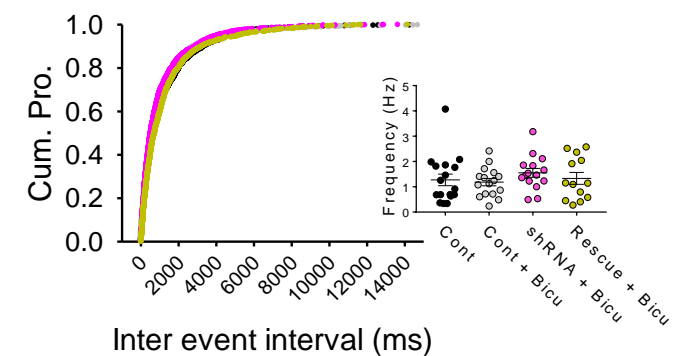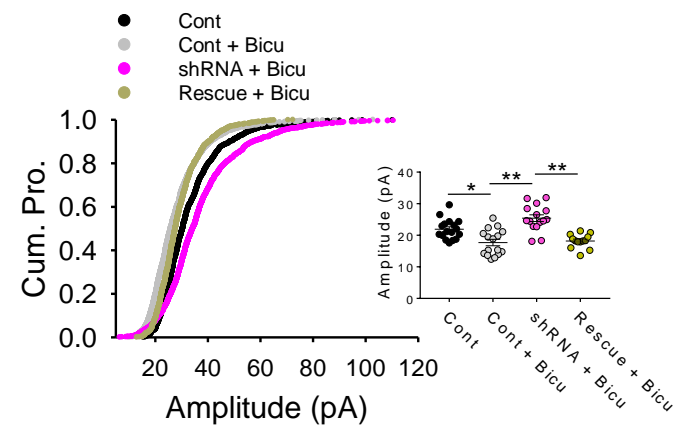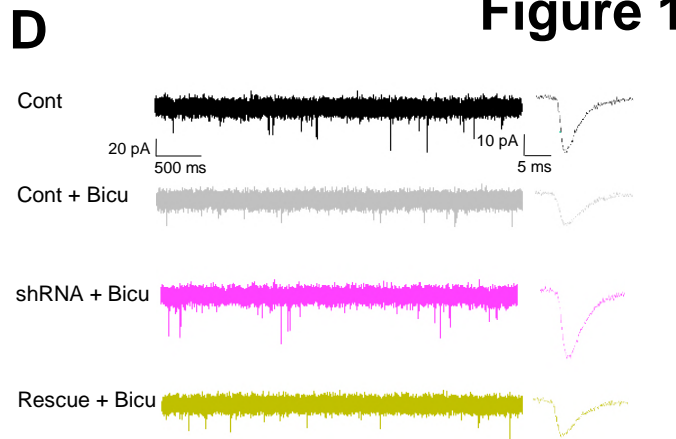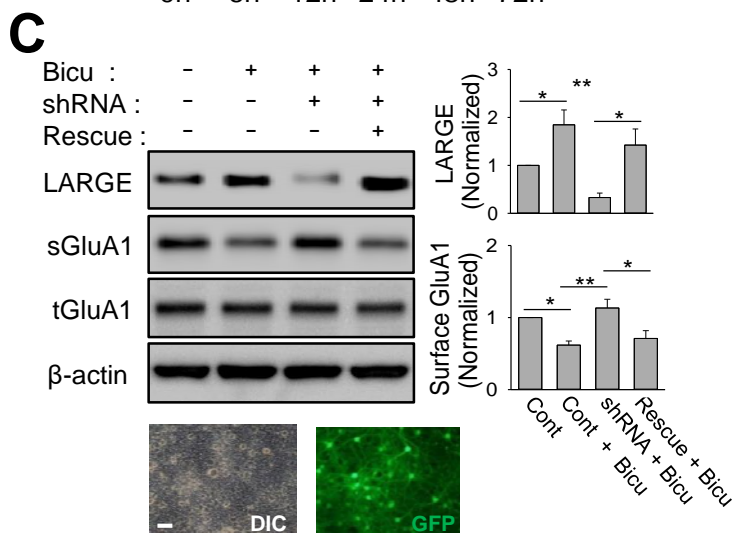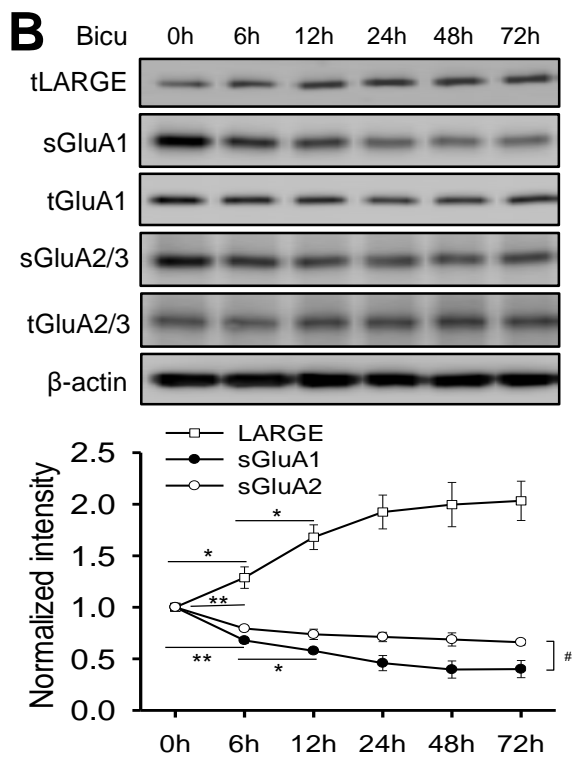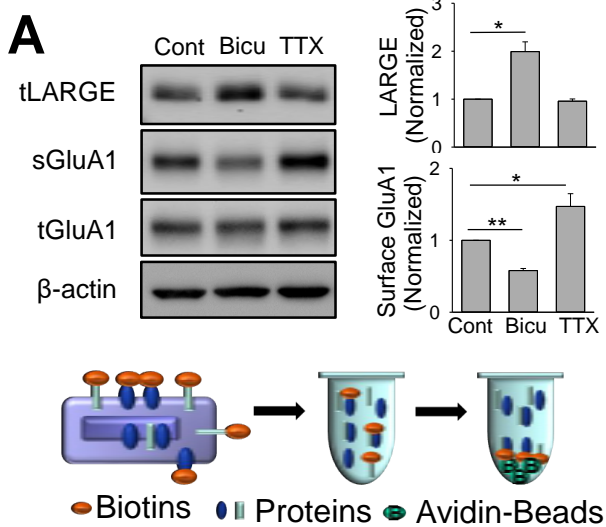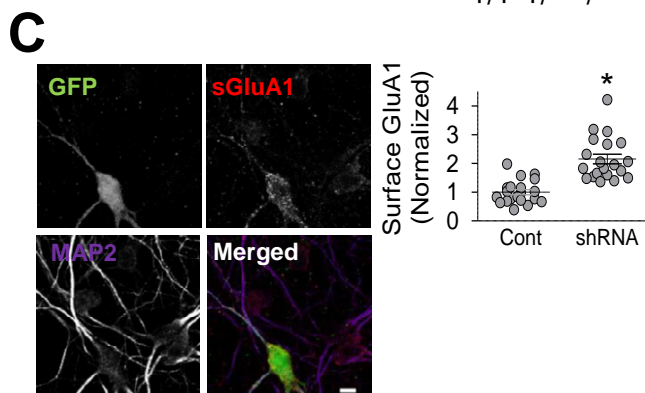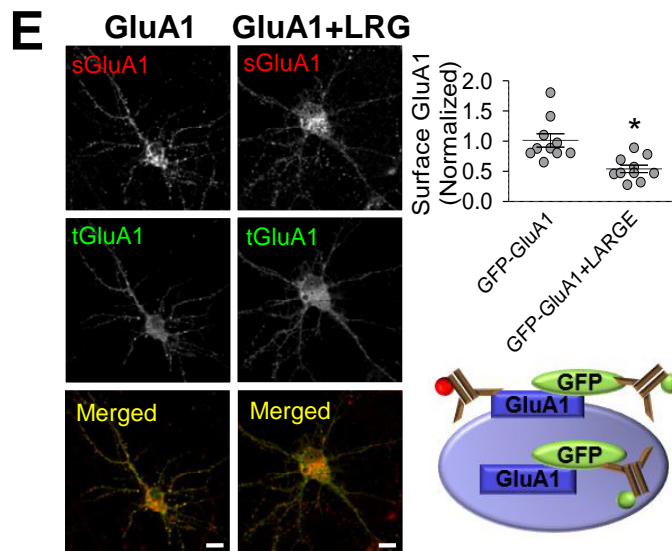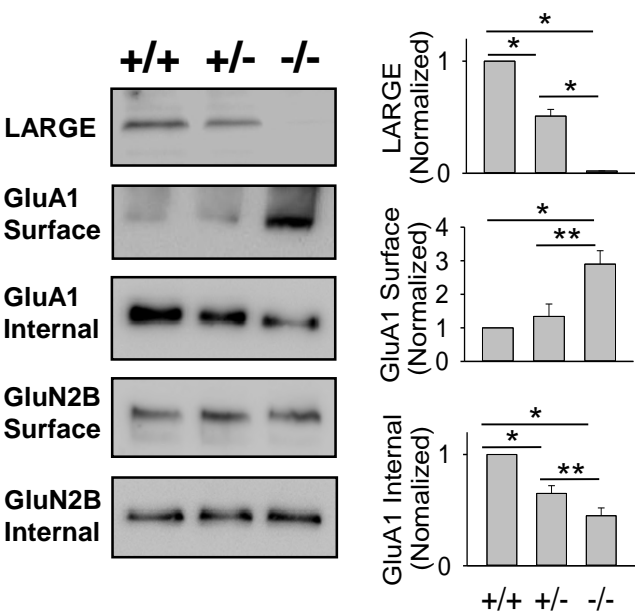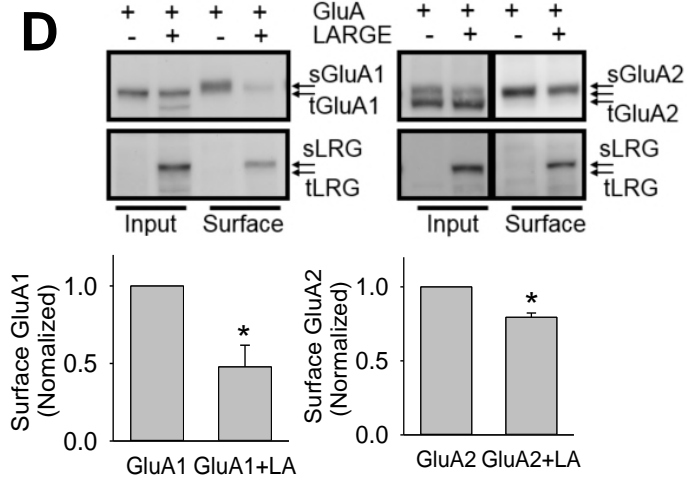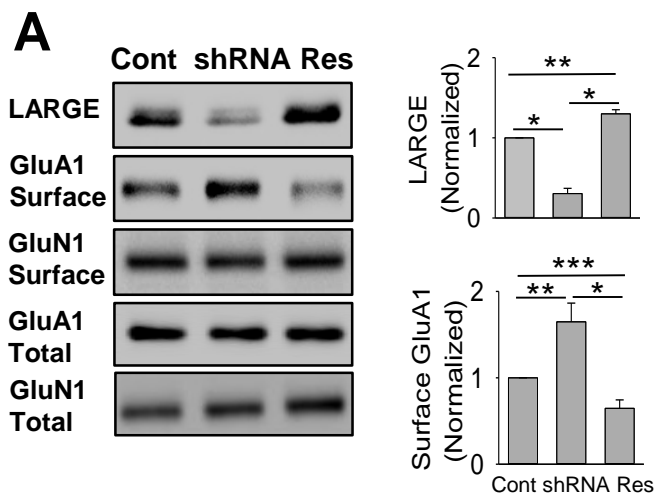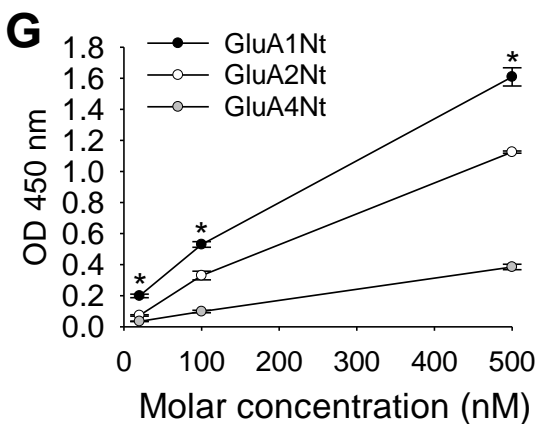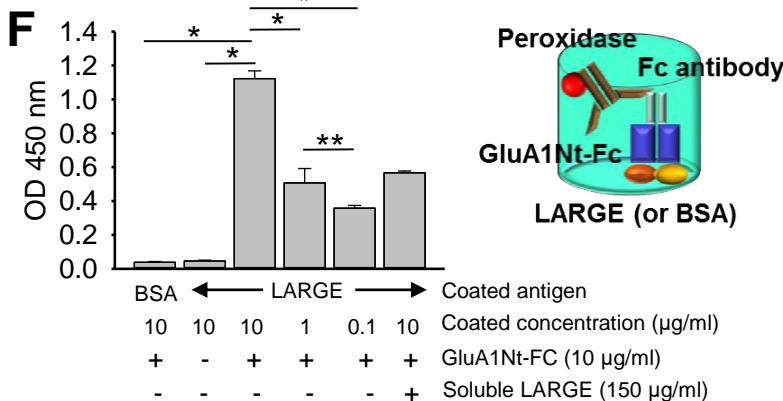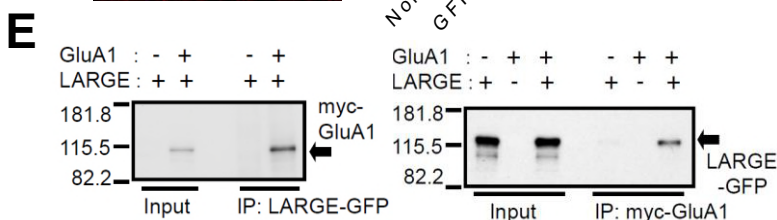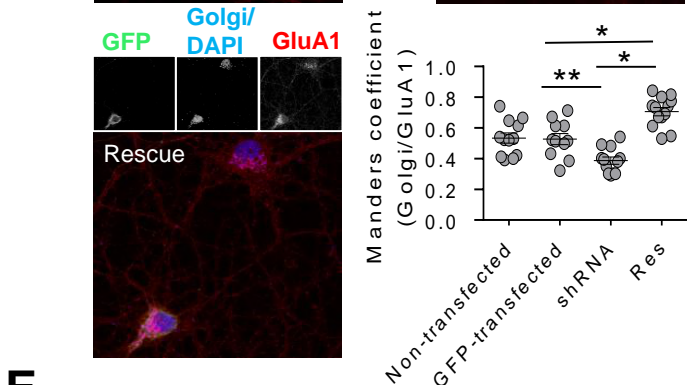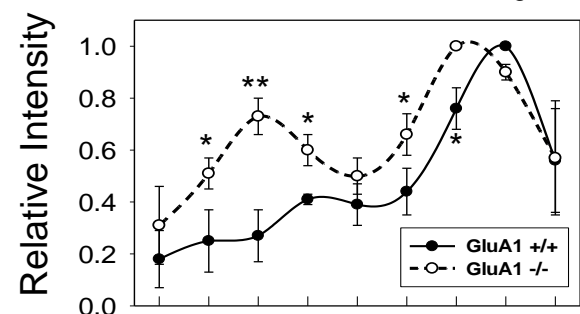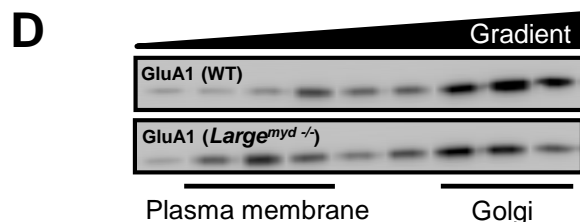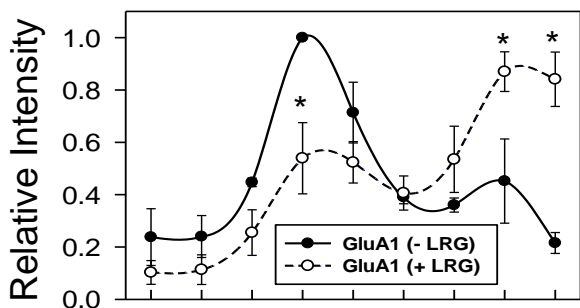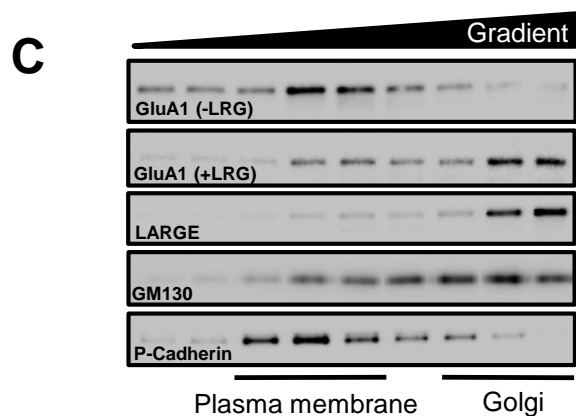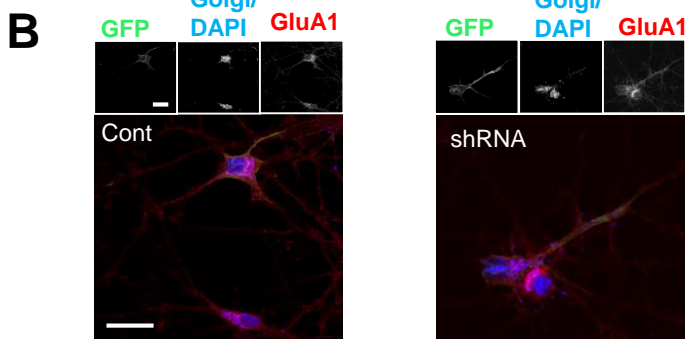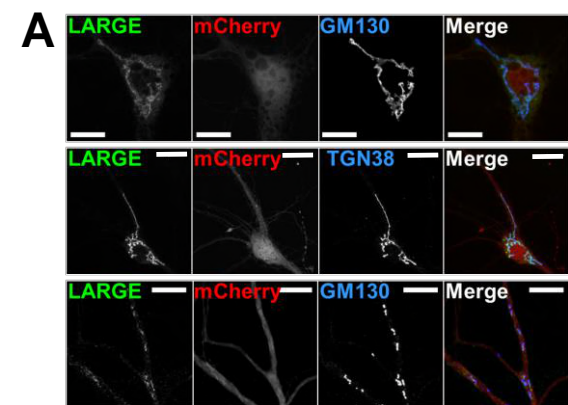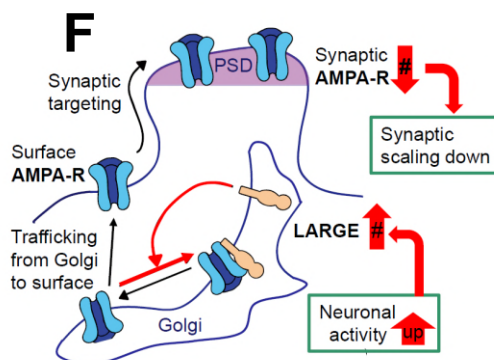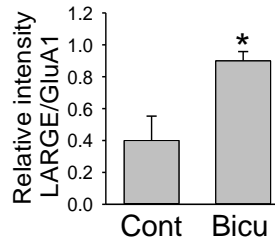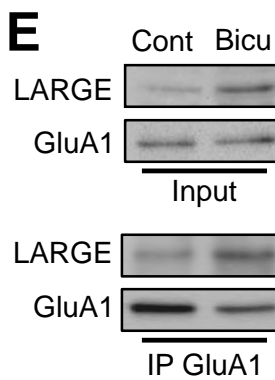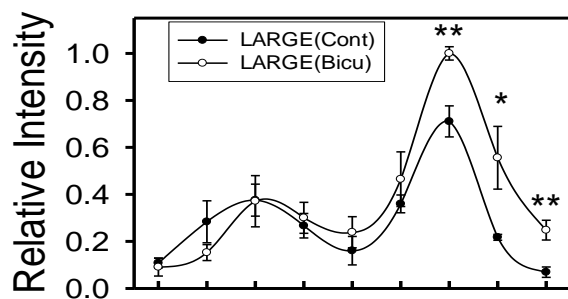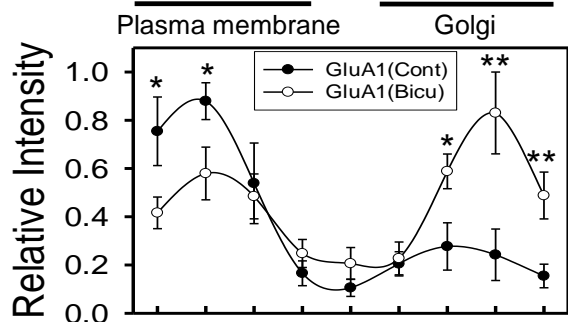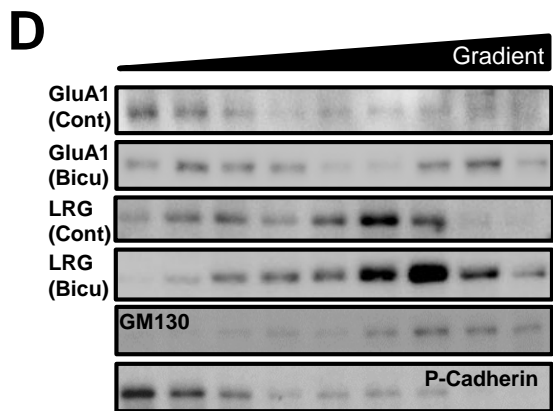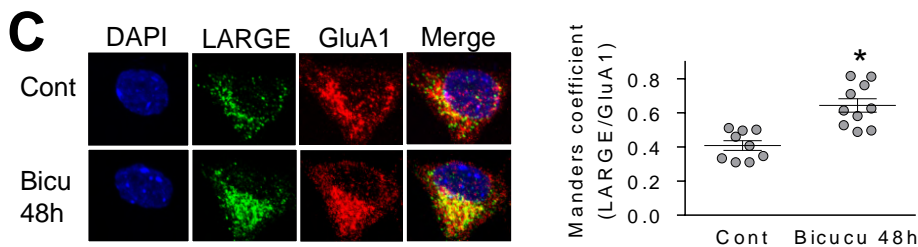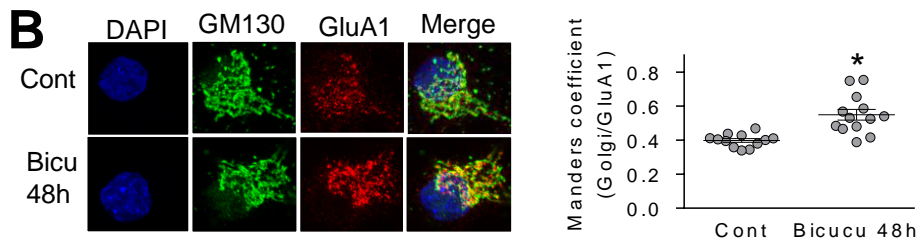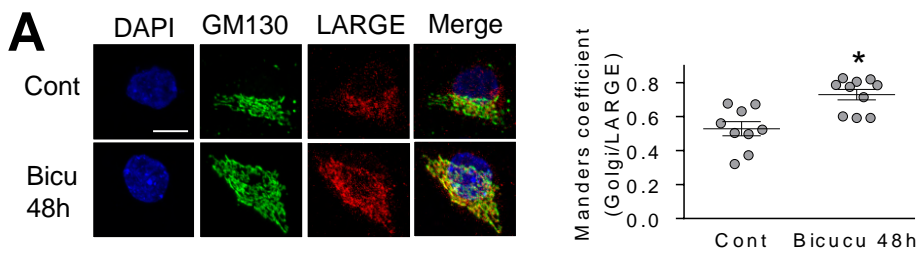
Figure 5

Figure 6

Figure 7

A Open Field

B Working Memory
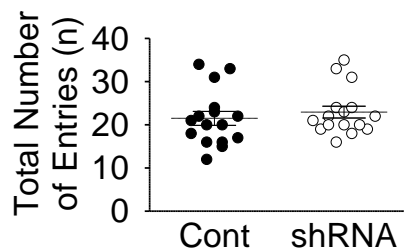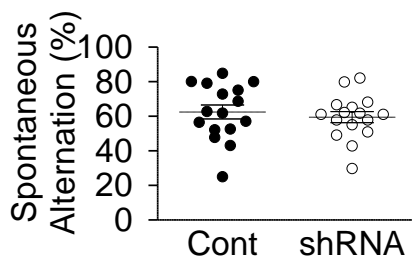
C Simple novelty preference

ITI 1min

Arm Entries #

Time in Arm

ITI 24h

Arm Entries #

Time in Arm

D Novel Object Recognition

Training

Short Term (5 min)

Long Term (24h)
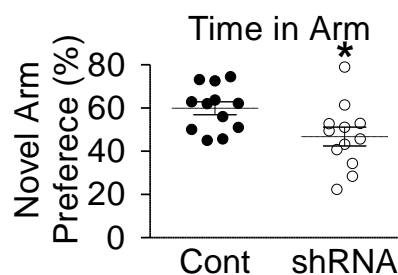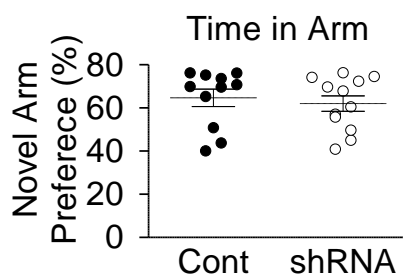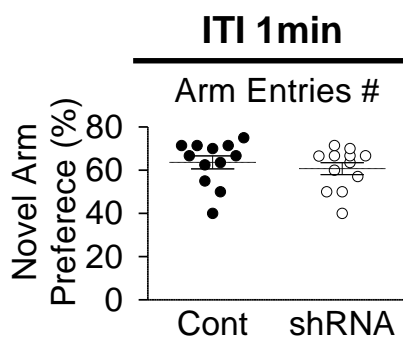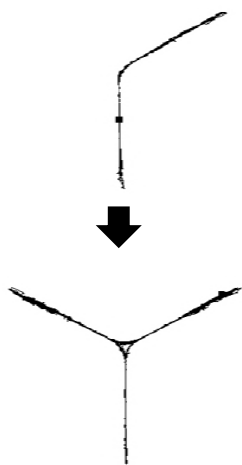
Figure 1-figure supplementary 1

Figure 1-figure supplementary 1. Validation of AAV expressing *LARGE* shRNA with GFP. (A) A representative fluorescence image of GFP signals demonstrated that most cultured hippocampal neurons were infected by the AAV. (B) Differential interference contrast (DIC) image shows the number and shape of neurons in the culture. These live images were recorded with 20x objective attached to a Nikon TMD inverted microscope system connected to a Nikon digital camera system (Digital-Sight DS-2Mv). (C) Western blot analysis confirmed knockdown of *LARGE*. Scrambled shRNA was used as control (Cont) (n=3, two tailed t-test, *$P < 0.005$). Scale bar = 100 μm.
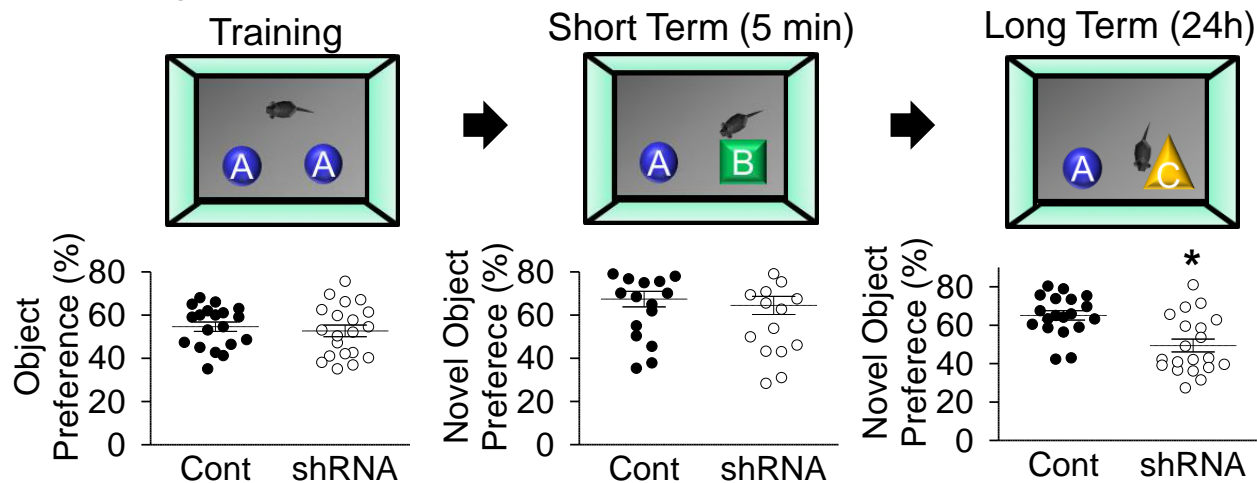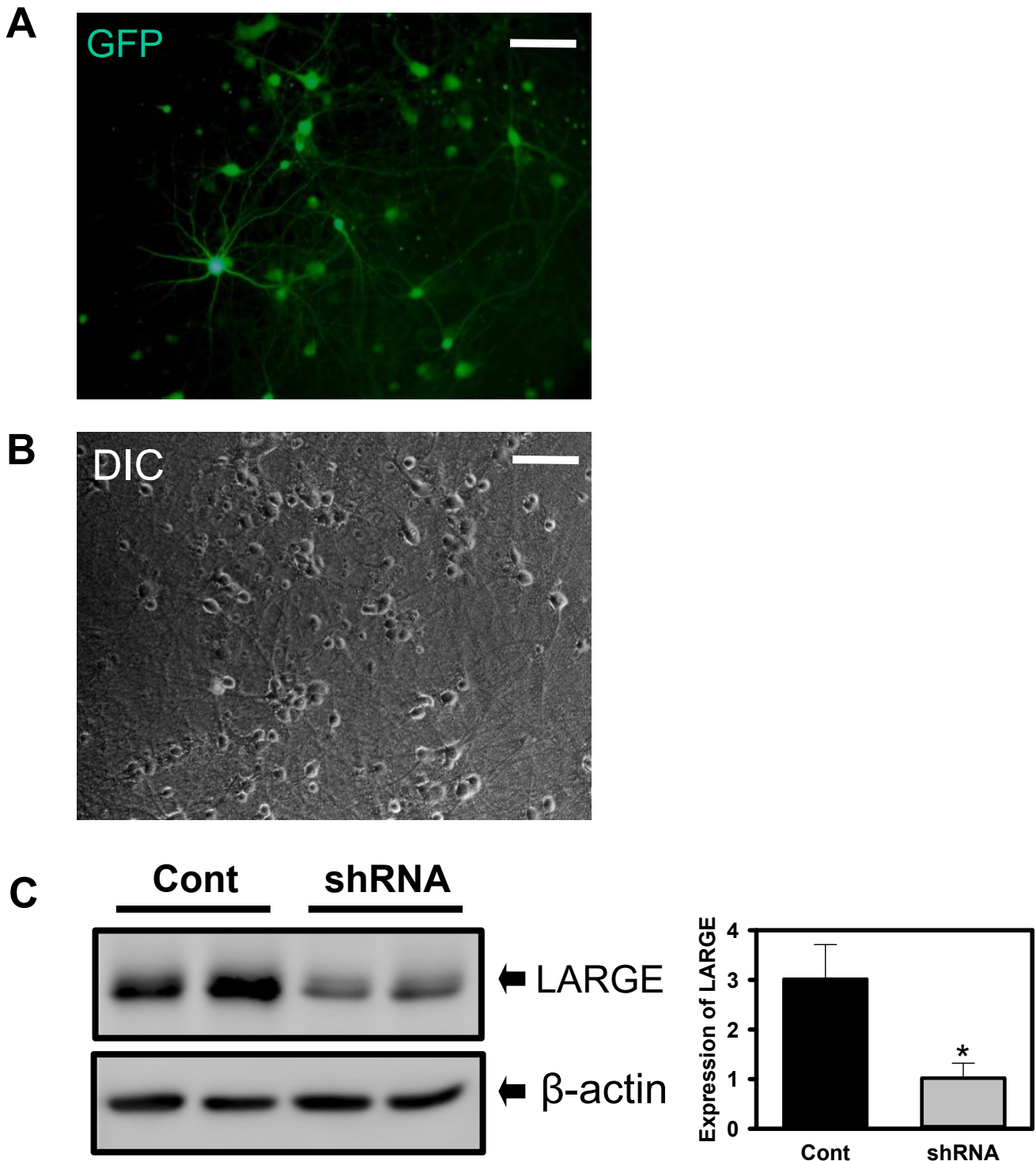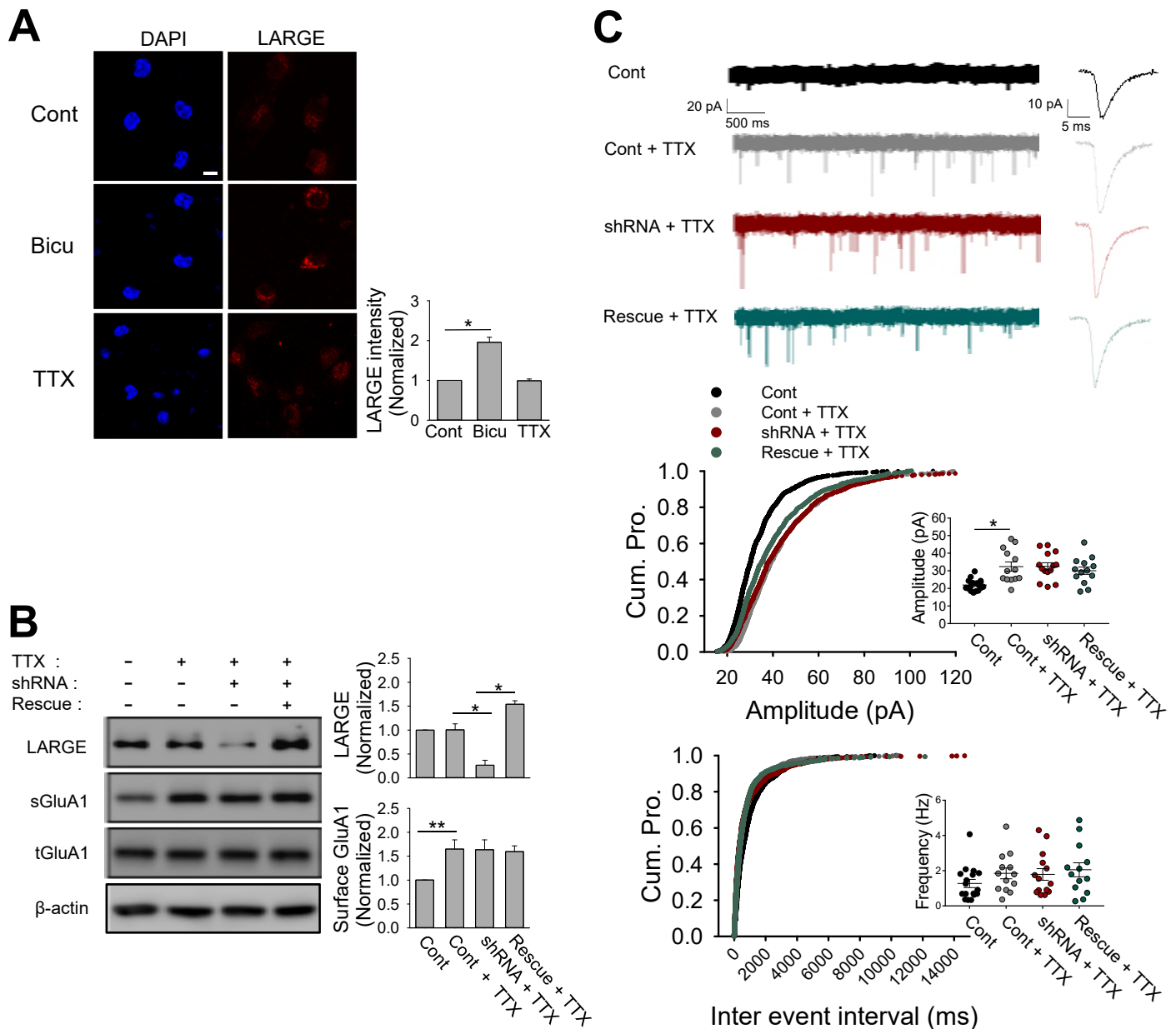
Figure 1-figure supplementary 2

Figure 1-figure supplementary 2. LARGE is necessary for neuronal homeostatic scaling-down but not for scaling-up. (A) Confocal images of cultured hippocampal neurons confirmed the increase in LARGE expression in response to Bicu but not TTX (n = 13, 13, 13 neurons; Mann–Whitney rank sum test, T = 91, U = 0, *P <0.001; Blue: DAPI, red: endogenous LARGE). Scale bar = 10 μm. (B) The TTX-induced increase in surface GluA1 was not affected by LARGE shRNA or LARGE rescue. (n = 3; one-way ANOVA, *P <0.001, **P = 0.027). (C) The TTX-induced increase in mEPSC amplitude was not affected by LARGE KD or rescue (1300, 1270, 1300, and 1279 events from n = 17, 13, 14, and 13 neurons, respectively; one-way ANOVA; amplitude, F(3,53) =7.783, *P <0.001; frequency; F(3,53) =1.211, P = 0.315). The mEPSC traces and cumulative and scattered plots are shown. Nine different groups were recorded using 60 coverslips from three batches of neuronal culture.
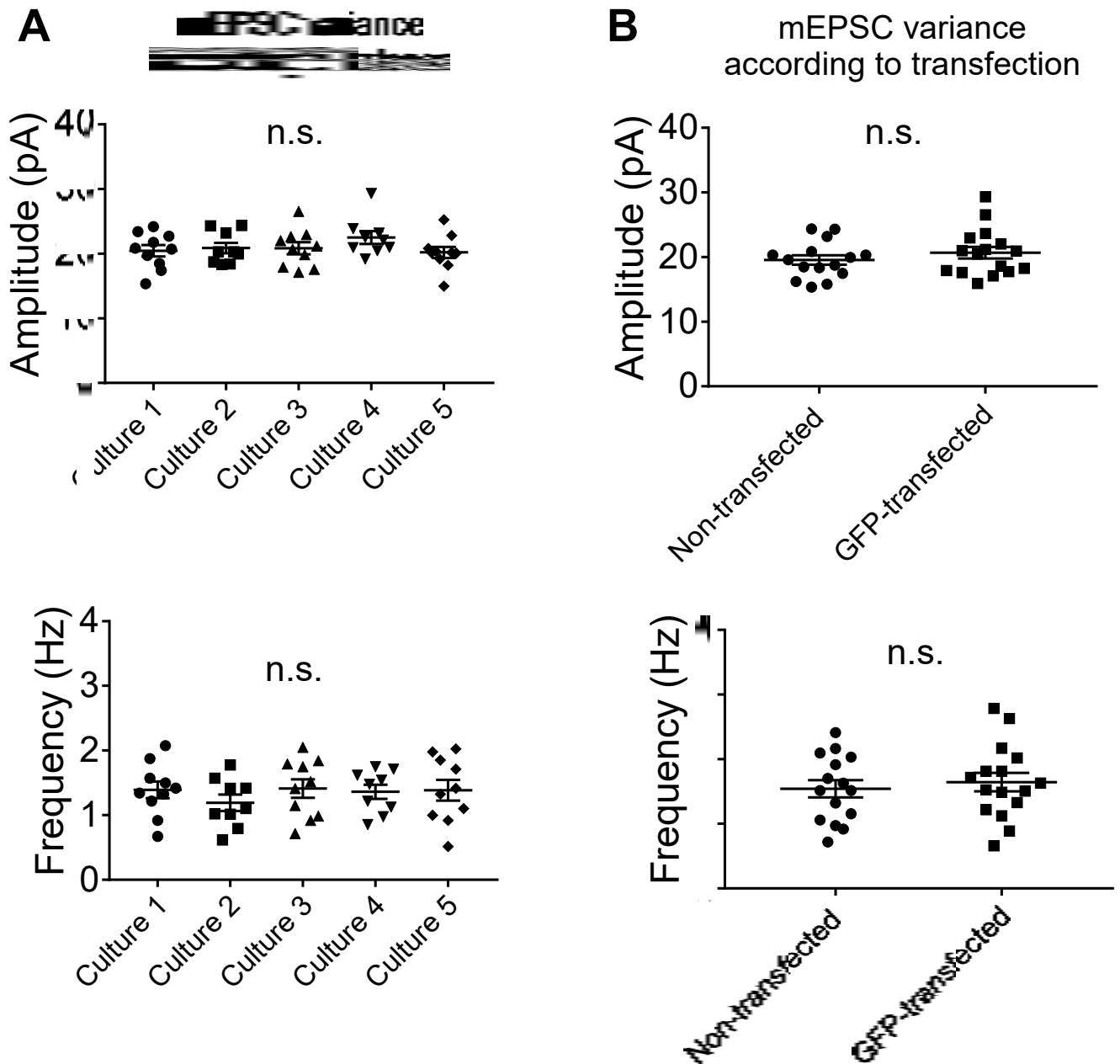
Figure 1-figure supplementary 3

Figure 1-figure supplementary 3. Verification of low-level batch-to-batch variation in our mEPSC experiments. (A) The amplitude and frequency did not vary among the batches used in experiments (B) The amplitude and frequency did not vary between non-transfected and GFP-transfected neurons

Figure 3-figure supplementary 1

A

B

Figure 3-figure supplementary 1. LARGE increased AMPA-R pool in the Golgi. (A) GFP-GluA1 in Golgi was increased by LARGE overexpression (GluA1 + LRG), compared with a control (GluA1) (n = 30, 30 cells; Two tailed t-test, *P < 0.001). Co-localization of GluA1 with GM130 in HEK293T cells analyzed by 3D reconstruction of a series of z-stack confocal images. Complete (yellow) and partial co-localization (orange). Co-localization of GluA1 and LARGE was quantified using the co-localization analysis tool in the NIS-Elements software (Nikon). In the analysis, Manders overlap coefficients were given and used to obtain the relative co-localization values between those two proteins. Scale bar = 10 μm. (B) Fractionation of subcellular organelles from the hippocampal CA1 of mice. Representative data showing the fractionation of organelle markers and LARGE. P-cadherin, plasma membrane marker; GM130, Golgi markers.
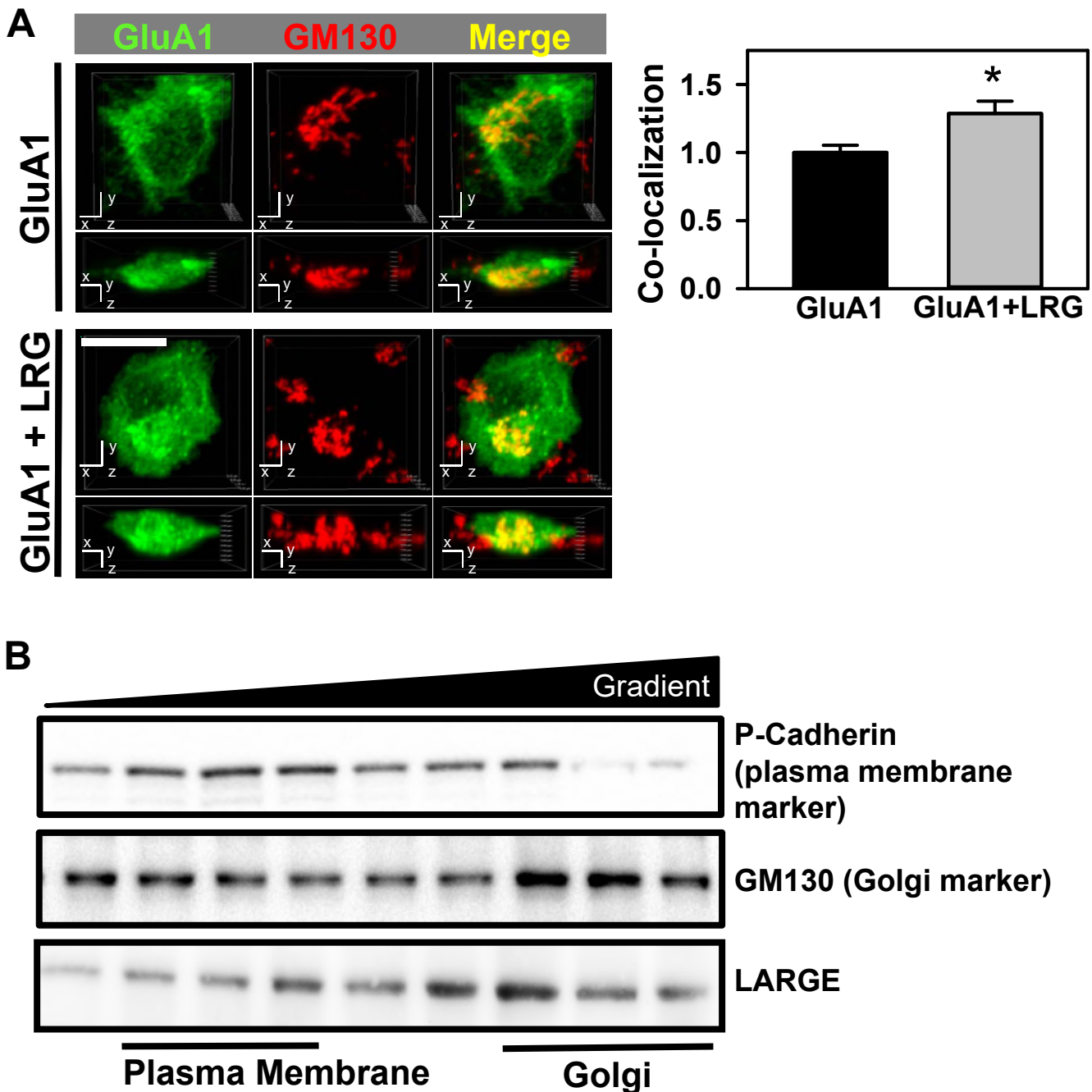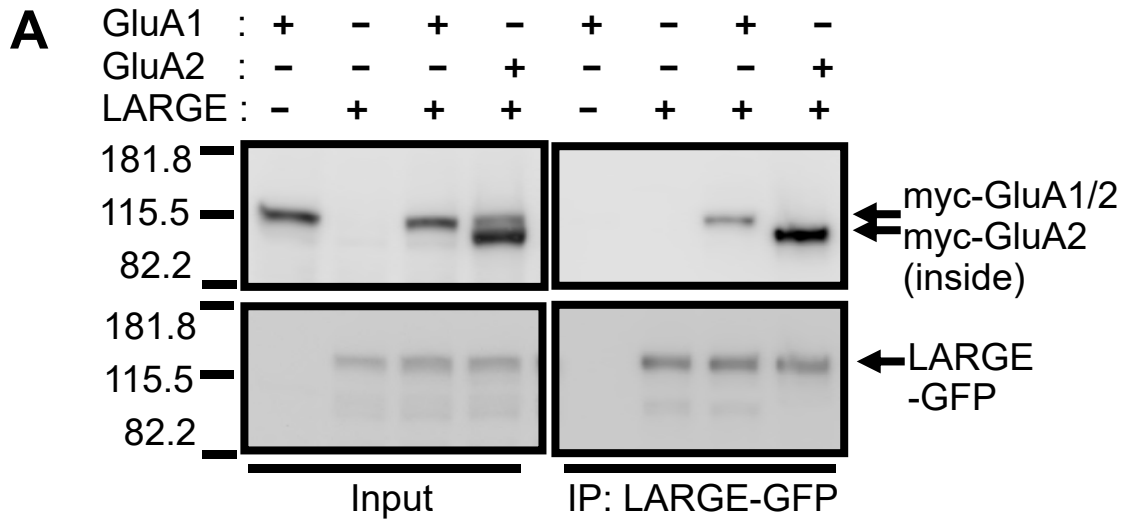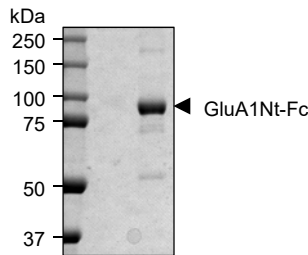
Figure 3-figure supplementary 2

A

GluA1 :	+	−	+	−	+	−	+	−
GluA2 :	−	−	−	+	−	−	−	+
LARGE :	−	+	+	+	−	+	+	+

myc-GluA1/2
myc-GluA2
(inside)

LARGE
-GFP

Input   IP: LARGE-GFP

B   GluA1Nt-Fc

C   GluA1Nt-Fc

D   LARGE ectodomain (CD1 + CD2)

E   LARGE ectodomain (CD1 + CD2)
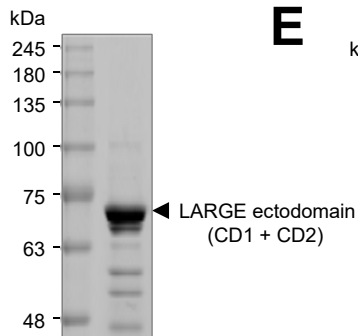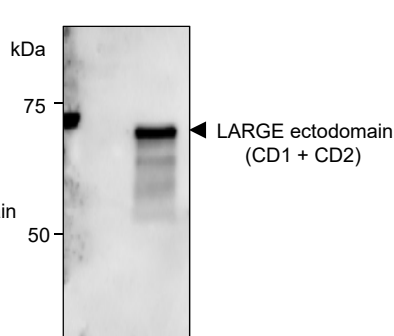
Figure 3-figure supplementary 2. LARGE directly interacts with AMPA-R subunits. (A) LARGE interacted with GluA2 inside of cell (lower band) but not with GluA2 at the plasma membrane (upper band). Analysis of LARGE association with AMPA-R determined by immunoprecipitation (IP). HEK293T cells were transfected with myc-GluA1, myc-GluA2, and/or LARGE-GFP. IP with anti-GFP antibody. Both GluA1 and GluA2 were co-immunoprecipitated with LARGE-GFP. As see in Input, GluA2 yield two bands (upper and lower bands). Most GluA2 co-immunoprecipitated with LARGE was GluA2 correspond to intracellular GluA2, judging from its molecular weight. (B-E) Purification of GluA1 and LARGE (catalytic domain 1 [CD1] + CD2) proteins. SDS-PAGE (B) and Western-blot (C) analysis of purified GluA1Nt-Fc fusion protein. SDS-PAGE (D) and Western-blot (E) analysis of purified LARGE.

Figure 3-figure supplementary 3

GluA1 : + + + + + + + +
LARGE: – + – + – + – +

GluA1 ←
DG-A1 ←

Endo-F: – – + + – – – –
Endo-H: – – – – + + – –
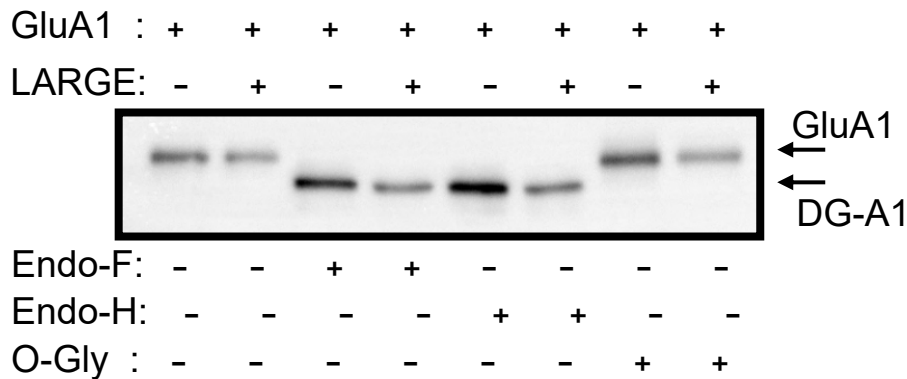O-Gly : – – – – – – + +

Figure 3-figure supplementary 3. LARGE interaction with AMPA-R did not change glycosylation of AMPA-R. No change in N- and O-glycosylation of GluA1 with co-expression of LARGE in HEK293T cells. N-linked glycosylation of GluA1 was analyzed using two de-glycosylation enzymes, endoglycosidase F (Endo-F) and endoglycosidase H (Endo-H). Endo-F completely de-glycosylated all GluA1 regardless of LARGE co-expression, and there was no difference in the amount of Endo-H–sensitive and –insensitive forms of GluA1 with co-expression of LARGE. In addition to N-linked glycosylation of GluA1, O-linked glycosylation of GluA1 was analyzed using O-glycosidase (O-Gly). The size of a GluA1 band was not changed by O-Gly treatment, suggesting that GluA1 does not have O-glycosylation. Co-expression of LARGE did not changed the O-glycosylation status of GluA1. Method: In HEK293T cells, myc-GluA1 and LARGE were expressed by transfection of their plasmids. From the lysate of the cells, myc-GluA1 was immunoprecipitated and treated with Endo-F (500 unit) and Endo H (500 unit) at 37℃ for 2 hours, or with O-Gly (50000 unit) followed with SDS-PAGE and Western blot analyses.

Figure 5-figure Supplementary 1
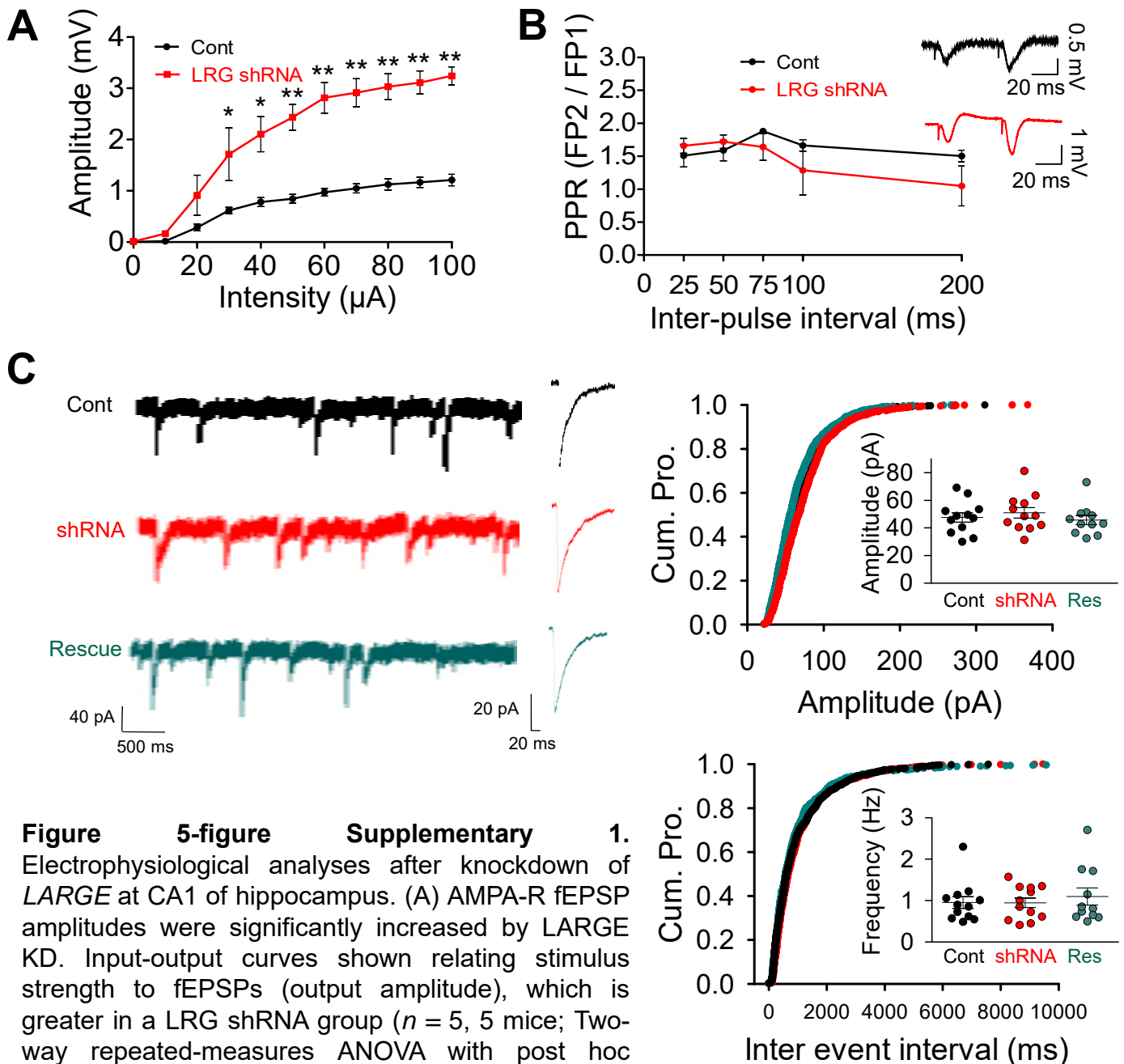
A

B

C

Figure 5-figure Supplementary 1. Electrophysiological analyses after knockdown of *LARGE* at CA1 of hippocampus. (A) AMPA-R fEPSP amplitudes were significantly increased by LARGE KD. Input-output curves shown relating stimulus strength to fEPSPs (output amplitude), which is greater in a LRG shRNA group (n = 5, 5 mice; Two-way repeated-measures ANOVA with post hoc Bonferroni t-test, *P < 0.05, **P < 0.001). (B) Intact short-term plasticity. Mean PPR (FP2/FP1) of fEPSPs plotted as a function of inter-pulse. Field potential (FP) data are mean ± s.e.m. (group: P = 0.565, group x interval: P = 0.170, n=5, 5).

(C) LARGE did not affect inhibitory synaptic strength. mIPSC recordings from Cont, shRNA, and Rescue. No significant differences in mIPSC amplitude and frequency were observed among the groups. Three different groups were recorded using 27 coverslips in 3 batches of neuronal culture (1098, 1080, 1055 events from n = 12, n=12, n=11 neurons, respectively; Amplitude, $F_{(2,32)}$=0.553, P =0.58; Frequency, $F_{(2,32)}$=0.292, P=0.749). Scale bar = 30 μm.

Figure 5-figure supplementary 2

Figure 5-figure supplementary 2. Confocal image analyses demonstrated the effect of *LARGE* KD on structural synaptic plasticity. Confocal images of cultured hippocampal neurons showed that *LARGE* KD (shRNA) significantly increase not the number of spines but the size of spines compared to that of control neurons, which was reversed by LARGE rescue (n = 7, 7, 7 neurons; One-way ANOVA, $*P < 0.01$, $**P < 0.005$). In the cultured hippocampal neurons, neuronal dendrites and spines was visualized by GFP. PSD95 is synaptic marker. MAP2 is dendrite marker. Scale bar = 10μm.
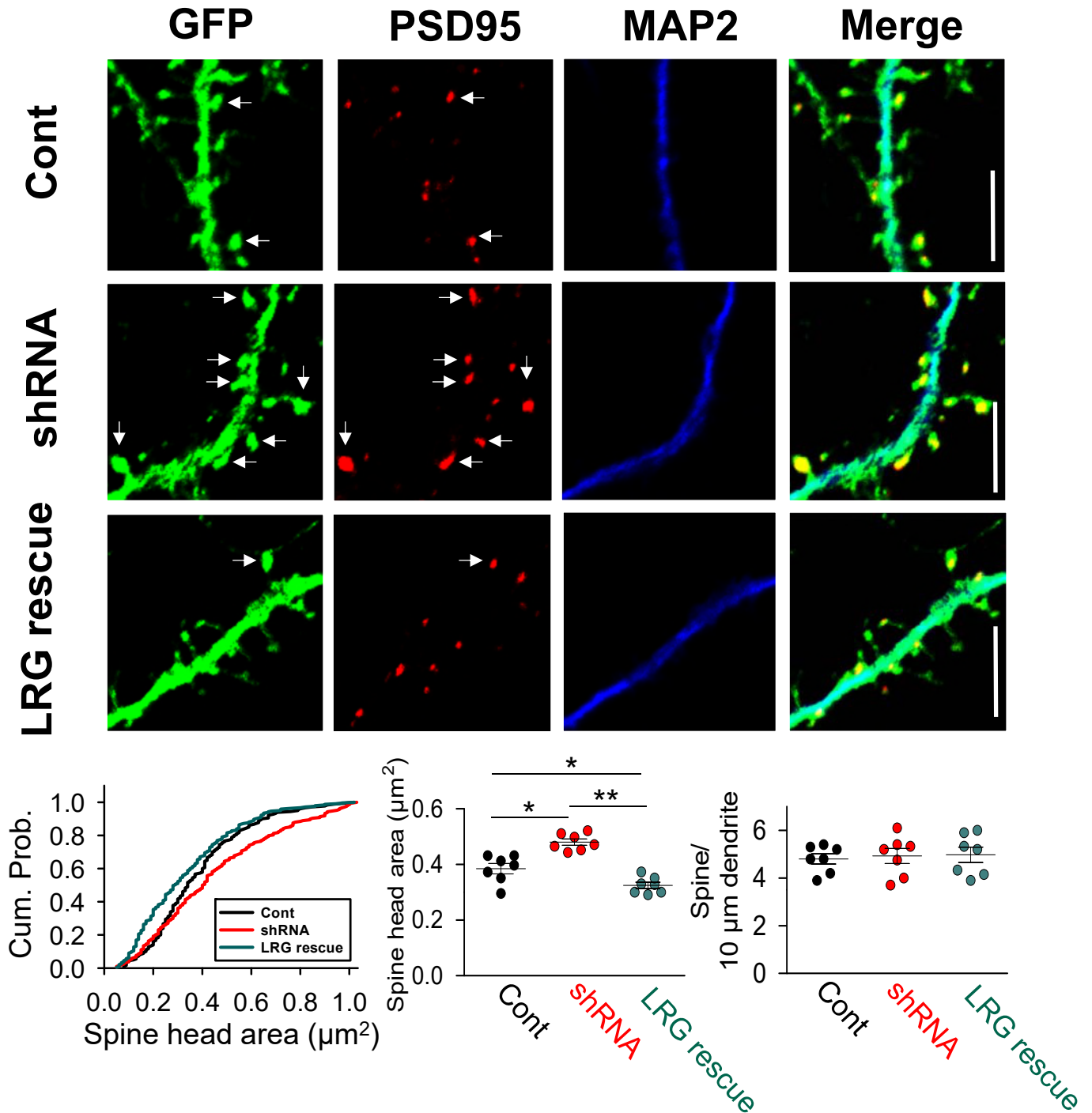
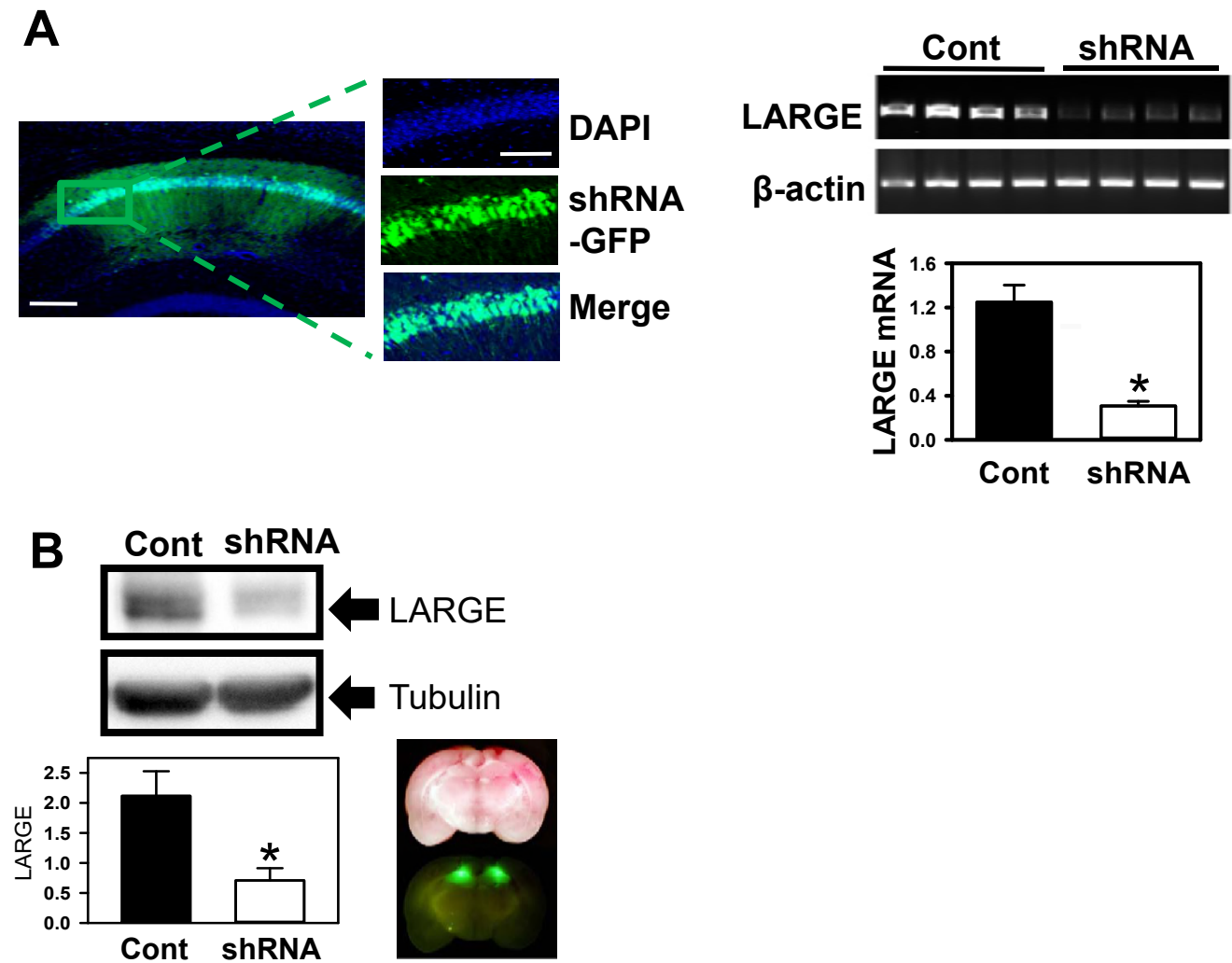# Figure 6-figure supplementary 1

Figure 6-figure supplementary 1 Confirmation of knockdown efficiency of LARGE shRNA after *in vivo* electrophysiology analyses and behavior tests. (A) Immunohistochemistry and RT-PCR analysis of mouse hippocampal CA1 region infected with AAV. Confocal images showed the location and diffusion range of AAV microinjected into CA1. Endogenous *LARGE* mRNA expression in CA1 was significantly knocked down by infection of AAV expressing *LARGE* shRNA with GFP (shRNA) (n = 3, 3 mice; Two tailed t-test, *P < 0.001). Scale bar = 100 μm (left), 50 μm (right). (B) Digital image and Western blot analysis of hippocampal CA1 region of rat brain infected with AAV. Brain slices were imaged by digital imaging under a blue LED light. Strong and specific expression of GFP in hippocampi indicated specific delivery and expression of *LARGE* shRNA with GFP by AAV injection. Western blot analyses confirmed knockdown of *LARGE* in GFP-expressing hippocampi (*n* = 3, 3 rats; Two tailed t-test, *P < 0.005)

Figure 6-figure supplementary 2

A

Time = 0 Shock Time = 4:28 Shock Time = 4:58 Time = 10:30

B

LARGE KO

LARGE Knockdown
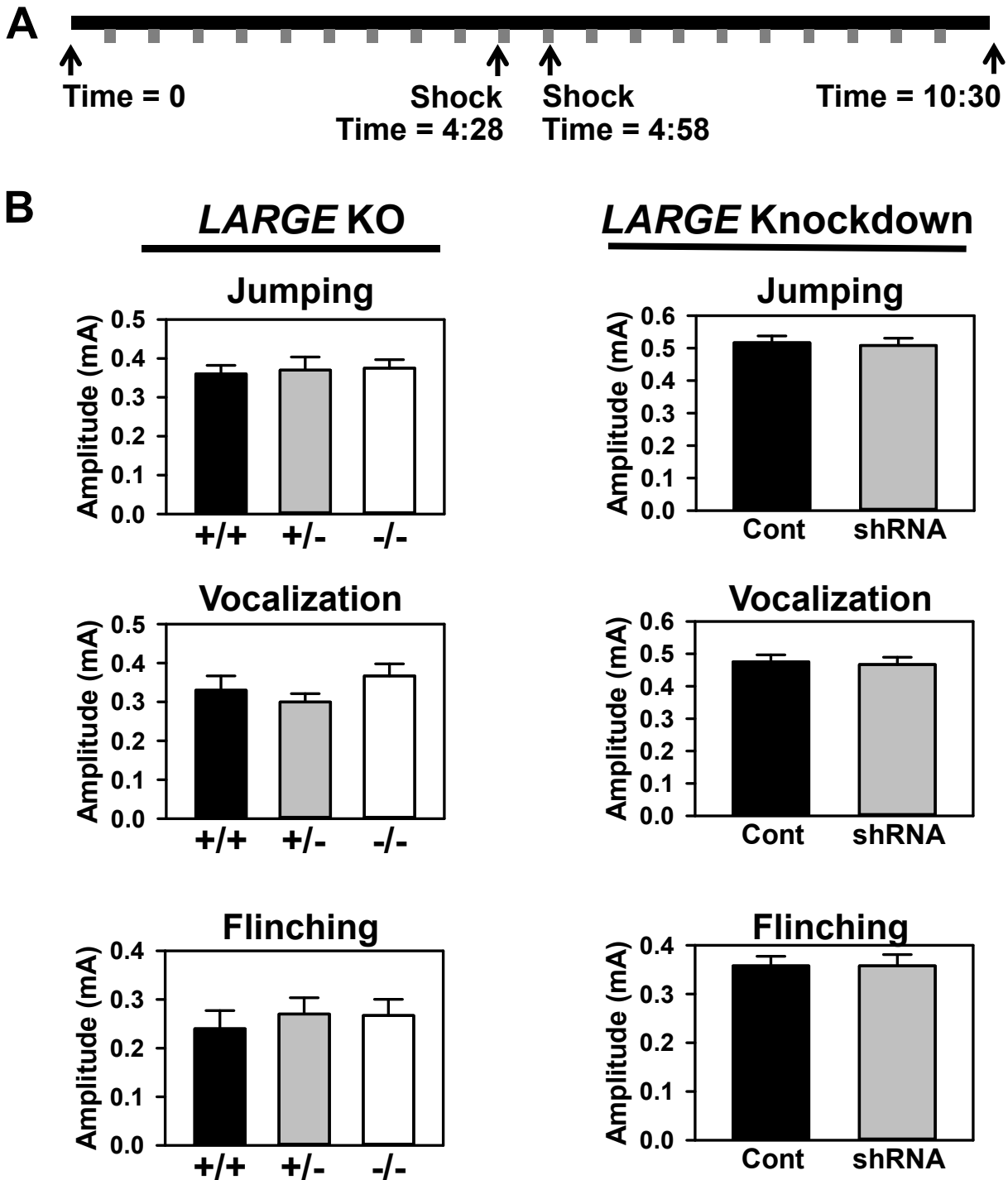
Jumping — Vocalization — Flinching

Figure 6-figure supplementary 2 The absence of a significant difference in shock threshold among groups demonstrated that LARGE expression status did not affect fear conditioning. (A) Schema of shock threshold tests of animals. Shocks (gray blocks) were delivered every 30 s, with intensity increasing from 0.1 mA to 1.0 mA (4:28, 4:58) and decreasing back to 0.1 mA (10:30). (B) Regardless of genotype or injected AAV, all animals responded to shocks in a similar way. The shock intensity thresholds for jumping, vocalization, and flinching were measured for wild type (+/+), heterozygous (+/-), and knockout (-/-) animals and animals injected with AAV expressing scrambled shRNA with GFP (Cont) or *LARGE* shRNA with GFP (shRNA).